


## Article

# Radon Dynamics in Granite and Calcareous Soils: Long-Term Experiments in a Semi-Arid Context

Sara Gil-Oncina <sup>1,\*</sup>, Concepcion Pla <sup>2</sup>, Javier Valdes-Abellan <sup>2</sup>, Angel Fernandez-Cortes <sup>3</sup>  
and David Benavente <sup>1,\*</sup>

<sup>1</sup> Department of Earth and Environmental Sciences, University of Alicante, 03690 Alicante, Spain

<sup>2</sup> Department of Civil Engineering, University of Alicante, 03690 Alicante, Spain; c.pla@ua.es (C.P.); javier.valdes@ua.es (J.V.-A.)

<sup>3</sup> Department of Biology and Geology, University of Almeria, 04120 Almeria, Spain; acortes@ual.es

\* Correspondence: sara.gil@ua.es (S.G.-O.); david.benavente@ua.es (D.B.)

**Abstract:** Radon in soil poses a significant health risk when it accumulates inside dwellings. The estimation of radon potential is a difficult task due to the complex dynamics of radon within soil and its relations with the weather. This research focuses on the variability of radon activity, driven by environmental changes, assessed in two loam soils (loamy sand–granite soil and silty clay loam–calcareous soil) with different radium contents. We conducted an experiment with teow soil columns in a semi-controlled outdoor laboratory, in a warm semi-arid climate. We also examined the consequences of abundant rainfall on radon activity through artificial soil water content (SWC) experiment conditions. Statistical analyses reveal that SWC is the most significant parameter influencing radon activity in these experiments. Radon is proportional to SWC and inversely proportional to temperature, evapotranspiration, and pressure in both soils, while wind is negatively related only in the loamy sand soil. Based on our findings, we modelled radon potential considering different soils and climatic contexts. SWC influences radon potential by changing radon emanation, activity, and permeability, depending on the local soil texture and radium concentration.

**Keywords:** geogenic radon potential; soil moisture; gas permeability; forced conditions experiment; continuous radon time series; environmental radioactivity



**Citation:** Gil-Oncina, S.; Pla, C.; Valdes-Abellan, J.; Fernandez-Cortes, A.; Benavente, D. Radon Dynamics in Granite and Calcareous Soils: Long-Term Experiments in a Semi-Arid Context. *Appl. Sci.* **2024**, *14*, 5910. <https://doi.org/10.3390/app14135910>

Academic Editors: Efren Garcia-Ordiales and Miguel Ángel Álvarez Vazquez

Received: 11 June 2024

Revised: 1 July 2024

Accepted: 4 July 2024

Published: 6 July 2024



**Copyright:** © 2024 by the authors. Licensee MDPI, Basel, Switzerland. This article is an open access article distributed under the terms and conditions of the Creative Commons Attribution (CC BY) license (<https://creativecommons.org/licenses/by/4.0/>).

## 1. Introduction

Radon is a noble gas that comes from the uranium decay chain. Specifically, <sup>222</sup>Rn, the radiogenic isotope of <sup>226</sup>Ra of the <sup>328</sup>U chain, has the longest half-life (3.82 days) among radon isotopes, which makes it more useful for scientific research than the other two isotopes (<sup>220</sup>Rn and <sup>219</sup>Rn). Radon is widely used for understanding and predicting geological processes, such as volcanoes and earthquakes [1–3]. However, it also poses a health risk to humans, since the decay products of <sup>222</sup>Rn are solid, radioactive isotopes that remain attached to breathable particles and continue to decay in lung tissue. As a result, radon is the second most common cause of lung cancer [4–6].

A major source of radon is the soil (geogenic radon), which may migrate into dwellings and become a potential health hazard when it accumulates indoors for a long period. To assess the radon risk, the geogenic radon potential is used, which is calculated from radon activity and soil gas permeability field measurements [7,8]. Natural <sup>226</sup>Ra concentration in soils is also used to estimate radon instead of measuring it directly on the field. Geogenic radon potential is used for the creation of predictive indoor radon maps on a large scale, which provide a risk assessment of radon exposure [9–12]. Neznal et al.'s radon potential (RP) equation for building sites is the most used for a local scale [7]:

$$RP = \frac{C_{Rn}}{pk_g - 10} \quad (1)$$

where  $C_{Rn}$  is the measured radon activity in soil air ( $\text{Bq m}^{-3}$ ) and  $pk_g = -\log k_g$  ( $k_g$  is gas permeability in  $\text{m}^2$ ).

The dynamics of radon in soil are complex and conditioned by several factors, such as parent material, mineralogy, porosity, organic matter, texture, water content, and gas permeability [13–17]. On the one hand, the higher the uranium content of the parent material, the higher the radon activity. However, it is also necessary to consider the microscopic-scale distribution of uranium within the mineral grains resulting from the consecutive phases of pedogenesis [18]. On the other hand, soil physical properties such as pore size and soil water content (SWC) affect the emanation and diffusion coefficients of radon, and therefore soil gas permeability in unsaturated systems [19–22]. Therefore, changes in soil gas permeability have a key role in reducing or enhancing radon migration outwards, while soil type is a decisive factor when characterising radon in soil [23–27].

In addition, weather parameters play a fundamental role by affecting the soil parameters mentioned above, as well as conditioning the development of the soil itself. A similar soil parent material may derive into different soils due to, for instance, more humid or arid climates [28]. Also, this difference in climatic context conditions the daily and seasonal weather, affecting geogenic radon potential [29,30]. In the short term, barometric pressure, temperature, wind, and evaporation are weather parameters associated with changes in radon dynamics [31–34]. Generally, a local high wind speed, a decrease in barometric pressure, and/or an increase in temperature lead to a decrease in radon activity [12,35,36].

Furthermore, soil and environmental variables, such as water content, also modify  $\text{CO}_2$  production and migration within the soil [37]. A great variety of studies in geosciences, including vulcanology and GHG soil emissions to the atmosphere or cave sites, among others, use  $\text{CO}_2$  together with radon as tracer gases [38,39], even though they have different origins. Organic  $\text{CO}_2$  is mainly formed in soils either by the proliferation and subsequent decomposition of microorganisms, or by the respiration of plants through their roots [40].

Many studies have been carried out to understand the relationship of radon with fractures and fault areas, and weather variables [41–45] with a closer perspective under controlled conditions—e.g., Haquin et al. [46], Nassiri-Mofakham et al. [47], and Papachristodoulou et al. [48]—but not deep enough to study the radon potential at a local scale.

Our research analyses the dynamics of radon for two types of soil, with different radium content and soil texture under a semi-arid climate (Alicante province, SE Spain). For this purpose, we developed an experimental procedure in semi-controlled, open laboratory conditions, where weather conditions and soil parameters were monitored.

First, recorded time series of all variables were examined to explore how weather and soil variables impact radon activity changes and to identify which ones are most decisive. Second, we performed an artificial soil water content experiment to further assess the effects of large rainfall on radon activity. Third, a detailed statistical analysis was performed to establish the correlations and weight of soil and weather variables related to radon. This analysis compared discrete rainfall events (with significant changes in radon activity) with the frequency response of long-term time series using wavelet analysis. Finally, based on our results, we evaluated radon activity and its response to weather parameters and soil properties in the context of radon potential estimation.

## 2. Materials and Methods

### 2.1. Weather Variables and Climate Series

According to the Köppen–Geiger classification, the study site has a Bsh hot semi-arid climate (hot steppe type; [49]). This climate classification defines climate scenarios on a global scale. Weather variables at the study site were provided by the Azotea IIG Station of the Climatology Laboratory-Interuniversity Institute of Geography of the University of Alicante, by a Davis Vantage Pro2 automatic weather station. The weather variables considered were relative humidity (%), barometric pressure (mbar), air temperature ( $^{\circ}\text{C}$ ), wind speed ( $\text{m s}^{-1}$ ), rain (mm) and evapotranspiration (ET, mm). ET is calculated directly by the

weather station with air temperature, environmental relative humidity, wind and radiation applying the Penman–Monteith Equation as implemented by CIMIS (California Irrigation Management Information System), which includes the calculation of net radiation.

For the period of monitoring, April 2021–February 2023, the average air temperature was 19.7 °C, reaching a maximum of 40.4 °C in summer and a minimum of 2.8 °C in winter. The average environmental relative humidity, barometric pressure and wind speed were 68.0%, 1017.2 mbar and 5.3 m s<sup>-1</sup>, respectively. The total rainfall was 435.2 mm while the calculated ET for the same period was 950 mm.

## 2.2. Soil Properties

The soils studied were chosen by their clear differences in terms of mineralogy and, therefore, differences in terms of geogenic radon potential: a silt soil from a calcrete, common in the Alicante region (Spain; identified henceforth as calcareous soil) that does not belong to a priority action area or a high-RP area according to the radon potential map of Spain [10]; and a second soil of weathered granite origin (granite soil hereafter) which belongs to the central area of Spain, classified as a priority action area. Additionally, they also represent two very different soil typologies that are at the same time representative of the context of the Spanish country.

Soil samples were taken, for both soils, from horizon A and horizon B separately. Horizons represent soil layers with different characteristics. They are arranged vertically in a soil profile. After that, columns of 50 cm diameter and 110 cm depth were prepared. The soil profile differs in both soils: calcareous soil has an AC profile, while the granite soil has an ABC profile. Therefore, the calcareous soil column only had horizon A, while the granite soil was prepared with horizon A (layer 1) to complete the first 55 cm, and the remaining 55 cm with horizon B (layer 2), as at the original location.

To characterise both soils, soil samples were prepared by removing gravel and root debris, followed by sieving. Soils were oven-dried at 40 °C for 24 h to determine dry bulk density (ratio of the dry weight to the volume of a sample). The grain density (particle or real density) was determined using an AccuPyc 1330 Helium pycnometer (Micromeritics Instrument Corporation, Norcross, GA, USA). Total porosity was obtained from grain and bulk densities. Soil particle size distribution was determined by hydrometer analysis according to the Spanish standard [50], and the soil texture type was obtained by the United States Department of Agriculture (USDA) classification. The granite soil was classified as a sandy loam and loamy sand type (horizons A and B, respectively), while the calcareous soil was classified as silty clay loam soil. Their initial characteristics are summarised in Table 1.

**Table 1.** Summary of the characteristics of the soils under study.

Initial Parameters	Calcareous Soil	Granite Soil	
		Layer 1 Horizon A	Layer 2 Horizon B
Bulk density (g cm <sup>-3</sup> )	1.25	1.68	1.55
Porosity (%)	52	35	42
Soil texture:	Silty clay loam	Sandy loam	Loamy sand
(%) sand	18	72	80
(%) silt	51	22	14
(%) clay	31	6	6
<sup>238</sup> U (Bq kg <sup>-1</sup> )	21.7	53.0	48.0
<sup>226</sup> Ra (Bq kg <sup>-1</sup> )	16.9	39.7	44.4

The determination of <sup>226</sup>Ra and <sup>238</sup>U radionuclides, performed by gamma spectrometry, demonstrates the higher uranium and radium content of granite soil compared to calcareous soil. The mineralogical composition, obtained with powder X-ray diffraction with a Bruker D8-Advance diffractometer (mirror Goebel, CuK $\alpha$  radiation—40 kV, 40 mA—2 $\theta$ : 3–60°, step size of 0.05°, scan step of 3 s; Bruker, Billerica, MA, USA), showed that the

calcareous soil is dominated by calcite, with a minor amount of quartz, dolomite, feldspar, and clay minerals. The mineralogical composition of horizons A and B of the granite soil is similar, composed of quartz, plagioclase, and feldspar. Horizon A presents higher amounts of clay minerals—e.g., kaolinite—derived from the alteration of a leucocratic granite, whereas horizon B shows a higher amount of muscovite.

### 2.3. Monitoring System

The experiments were performed in two experimental columns that contained the soils under study (Section 2.2). The columns were placed outdoors at the campus of the University of Alicante (Alicante province, SE Spain). This study was carried out in different periods depending on the soil: April 2021 to July 2022 for the granite soil, and July 2022 to February 2023 for the calcareous soil. Two different measurement periods were established because radon could only be measured continuously in one soil at a time.

The experimental procedure was identical for both columns. The columns consisted of a 110 cm high corrugated polyethylene tube with a 50 cm diameter (Figure 1). Several sensors controlled by dataloggers were installed providing continuous data on soil parameters through the studied period. The monitoring system consisted of a set of dataloggers (HOBO H22 (Onset, Bourne, MA, USA) and CR-1000 Campbell Scientific®—Logan, UT, USA) connected to the power supply and to a backup battery to prevent data loss. In each column, there were two different measurement points (at different depths; top and bottom, Figure 1) to continuously register the following at hourly intervals: (i) dielectric permittivity (to later calculate soil water content (SWC); accuracy:  $\pm 0.03 \text{ m}^3 \text{ m}^{-3}$  [51]); (ii) soil temperature (accuracy:  $\pm 1 \text{ }^\circ\text{C}$ ) using a 5TE automatic sensor (Decagon Devices, Pullman, WA, USA) connected to the CR-1000; and (iii)  $\text{CO}_2$  soil concentration GMP252 Vaisala CARBOCAP sensor (reading accuracy:  $\pm 2\%$ ; Vaisala, Vantaa, Finland), with a 0–10,000 ppm measurement range, connected to the HOBO H22. Note that the operating range of the  $\text{CO}_2$  sensor conditioned the measurement in the periods of highest soil  $\text{CO}_2$  production, mainly spring, since the probe was saturated, and real values were not available.

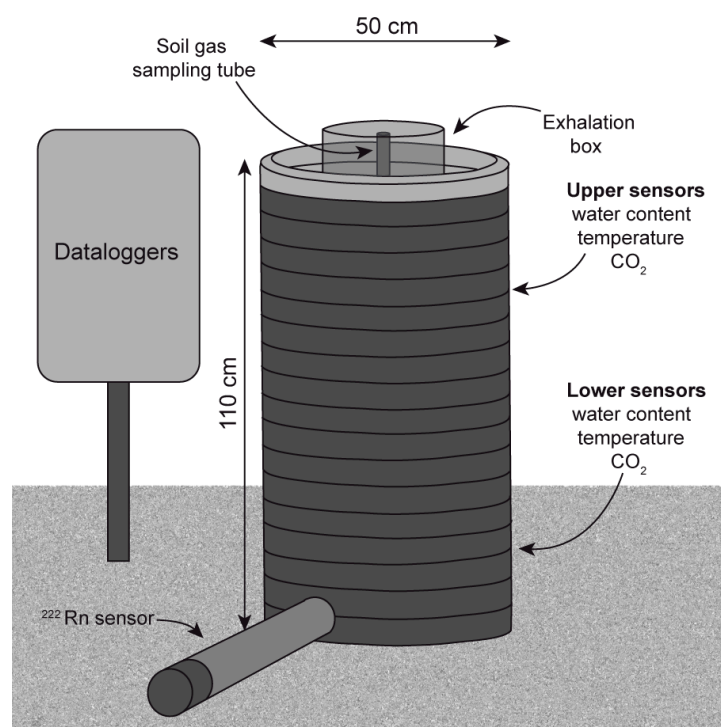


**Figure 1.** The general layout of the experimental setup of the sensors and dataloggers in the artificial soil columns.

In addition, at the bottom of each column (Figure 1), radon activity was continuously measured at 30 min intervals with a Barasol MC2 silicon detector (accuracy:  $\pm 50 \text{ Bq m}^{-3}$ ; Algade, Bessines-sur-Gartempe, France). This device was placed in a PVC-capped tube at the bottom of the column at the target soil depth of 90–100 cm, as radon and gas permeability measurements are usually performed at a 100 cm depth [50]. This is an adequate depth to avoid dilution of radon in soil due to mixing with atmospheric radon-poor air.

#### 2.4. Sampling System

Discrete sampling was carried out to calibrate the continuous series of radon and  $\text{CO}_2$ . A gas sampling tube was installed in each column at a depth of 90–100 cm—to achieve sampling at the target depth—to extract air from the soil (Figure 1).

Soil air samples were pumped out using a micropump and a 12 V battery and then collected in 2 L RITTER opaque gas sampling bags with lock valves (RITTER, Bochum, Germany). They were analysed with AlphaGUARD DF2000 (accuracy:  $\pm 3 \text{ Bq m}^{-3}$ ; Bertin Technologies SAS, Montigny-le-Bretonneux, Paris, France) at a  $0.3 \text{ L min}^{-1}$  pump flow and 1 min flow mode, for 15 min. The first six minutes of measurement, related to the time the gas sample needs to enter AlphaGUARD, were discarded and only the remaining 9 min were considered. This procedure only considers the measurement of  $^{222}\text{Rn}$  and avoids the  $^{220}\text{Rn}$  contribution ( $^{220}\text{Rn}$  half-life is 55.6 s), and therefore,  $^{222}\text{Rn}$  values recorded with AlphaGUARD are comparable to those with the Barasol device (which measures only  $^{222}\text{Rn}$ ).

The median radon value was corrected after measuring to compensate for the radon loss due to radioactive decay. Equation (2), based on the solution of Bateman equations, was used:

$$C_{Rn} = C_0 e^{-\lambda t}, \quad (2)$$

where  $C_{Rn}$  ( $\text{Bq m}^{-3}$ ) is corrected by applying  $\lambda = 0.00761 \text{ (h}^{-1}\text{)}$  for a particular time ( $t$ , h) [52] to obtain the actual radon activity in soil ( $C_0$ ,  $\text{Bq m}^{-3}$ ).

Radon exhalation rate ( $E$ ,  $\text{Bq m}^{-2} \text{ s}^{-1}$ ) was evaluated since it provides information on how soil releases radon to the atmosphere, which varies according to the soil type. We used an AlphaE sensor (sigma/24 h uncertainty:  $\pm 12\%$ ; Bertin Technologies SAS) inside a dust bag placed within a polymethyl methacrylate accumulation chamber (20 cm inner diameter and  $0.005 \text{ m}^3$  of effective volume). The accumulation chamber was placed on top of a PVC collar, completing the exhalation box, which was directly connected to the soil. Radon exhalation is calculated as follows (Equation (3)):

$$E = \frac{V C_{Rn}}{S t}, \quad (3)$$

where  $V$  ( $\text{m}^3$ ) and  $S$  ( $\text{m}^2$ ) are the effective accumulation volume and the exhalation surface of the soil within this accumulation chamber, respectively, at a particular time  $t$  (s).

Finally, soil gas permeability was measured with RADONJOK (Radon V.O.S., Praha, Czech Republic), and RP was estimated by applying Equation (1) by Neznal et al. [7]. Some discrete measurements of  $\text{CO}_2$  concentration were also performed using a CRDS analyser (Picarro G2201-i, Santa Clara, CA, USA).

#### 2.5. Artificial Soil Water Content Experiment

After continuous monitoring of both soils, we artificially increased the soil water content, aiming to simulate the natural water content increase associated with heavy rainfalls or flood irrigation.

The experiment involved the artificial addition of water in the granite (60 L) and calcareous (43 L) soil columns. In the case of the granite soil, the 60 L was added in 3 stages of 20 L each: 20 L at the beginning of the experiment, 20 L after 6 h, and 20 L after 22 h. For the calcareous soil, 43 L of water was added in 20 L at the beginning, 13 L after two days, and 10 L after five days. The experiments for the two soil columns were not

simultaneous due to the use of a single measuring device. Thus, as the water was added to the soil, the continuous monitoring system installed in the soil columns registered the soil variables explained in Section 2.3, as well as the radon exhalation rate (Figure 1). In these experiments, discrete sampling and continuous monitoring were carried out according to the methodology explained in Sections 2.2 and 2.3. A smoothing analysis was applied to the continuous series of radon activity, using the Adjacent-Averaging method with 15 window points.

### 2.6. Time Series Analysis

The analysis of radon activity alongside soil and weather variables considered the detection and analysis of discrete events with significant variations in radon activity, and the frequency response of the variables by wavelet analysis.

The statistical analyses of the discrete events were carried out in two steps. First, we defined the discrete events when significant variations in radon activity occurred. The analysed events were selected within the time series because they experienced significant variations in radon activity, generally 0.15% higher than average levels. We then evaluated all variables before and after rain episodes to find out which were the most decisive on soil properties and radon activity. This study examined granite soil because it presents a sandy texture, and consequently, major variations in all variables were expected due to changes in weather conditions.

Based on the results of the previous analysis, the second step consisted of a global analysis of the time series for both soils by selecting periods with no gaps in the continuous time series. To develop these analyses, the average daily values were obtained from the hourly recorded values of all measured variables.

Principal component analysis (PCA) and multiple linear regression analysis (MLR) were applied to the obtained datasets. PCA reduces the size of the number of variables initially considered and establishes associations between those variables that are organised into components. In the MLR analysis, radon in soil acts as a dependent variable, whereas soil and weather parameters serve as independent variables. This analysis also includes the weight (magnitude of the standardised coefficients, Beta) of each independent variable in the calculation of multiple linear equations, aiming to quantify the influence of each variable on radon activity. The  $p$ -value is obtained to evaluate which variable is most significant in the fitted regressions. The lower the  $p$ -value, the greater the statistical significance of the variable analysed. Statistical analyses were performed using the SPSS v.24.0 (SPSS Inc., Chicago, IL, USA).

To complement the analyses and assess the influence of soil variables on radon activity, the cross wavelet transform (XWT) and the wavelet transform coherence (WTC) were applied between pairs of signals (one being the soil radon activity). This time–frequency analysis allows us to examine the interrelations between two time-domain signals (explained by XWT) and their coherence (WTC), leading to the identification of areas with high common power between the pair of signals in the final scalograms [53–56]. Wavelets are a tool that helps in detecting periodic patterns in radon activity, which may be related to meteorological or environmental parameters [57]. For this analysis, the Environmental Wavelet Tool (EWT) MATLAB-based code [58] was used, which incorporates the package developed by Grinsted et al. [59]. This analysis was performed for the period October 2021–July 2022 for granite soil and from July 2022 to January 2023 for calcareous soil. These periods were established according to the data requirements for performing the wavelet analysis.

## 3. Results

### 3.1. Time Evolution of the Radon Activity and the Main Weather Parameters

Figure 2 (granite soil; April 2021–July 2022) and Figure 3 (calcareous soil; July 2022–February 2023) show the temporal evolution of all variables involved.

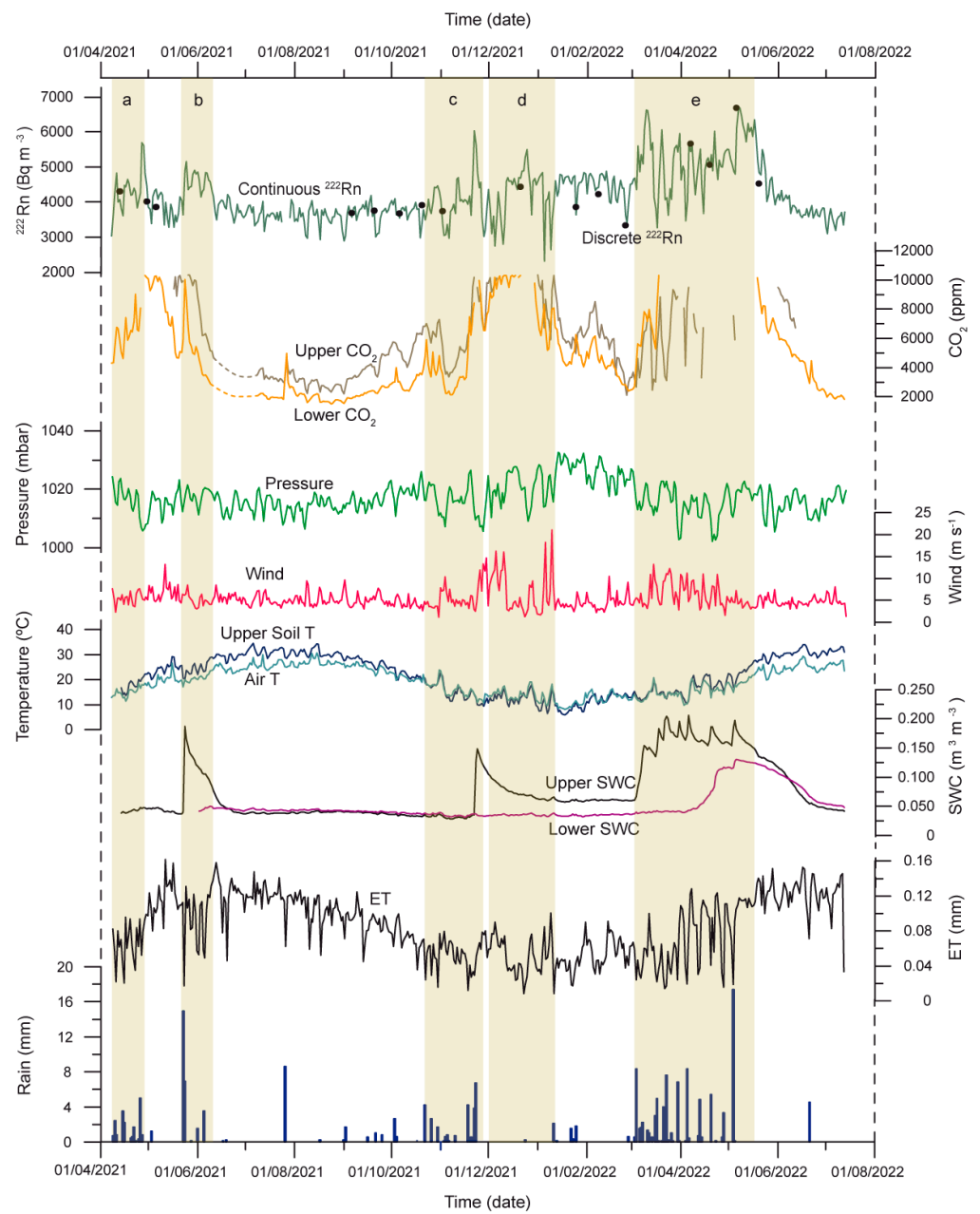


**Figure 2.** Daily temporal evolution of soil and weather variables in granite soil for the period July 2022–February 2023. The measured variables from bottom to top are as follows: rain (mm); evapotranspiration (ET, mm); continuous records of soil water content at the upper and lower layers of the soil column (SWC,  $\text{m}^3 \text{m}^{-3}$ ); continuous records of air and soil temperature at the upper and lower layers of the soil column (Air and Soil T,  $^{\circ}\text{C}$ ); continuous records of wind speed (Wind,  $\text{m s}^{-1}$ ); continuous record of pressure (P, mbar); continuous records of  $\text{CO}_2$  concentration at the upper and lower layers of the soil column (ppm); and discrete and continuous radon activity at the lower layer ( $^{222}\text{Rn}$ ,  $\text{Bq m}^{-3}$ ). The remarkable periods discussed in the text are highlighted in yellow, labelled as a, b, c, d, and e.

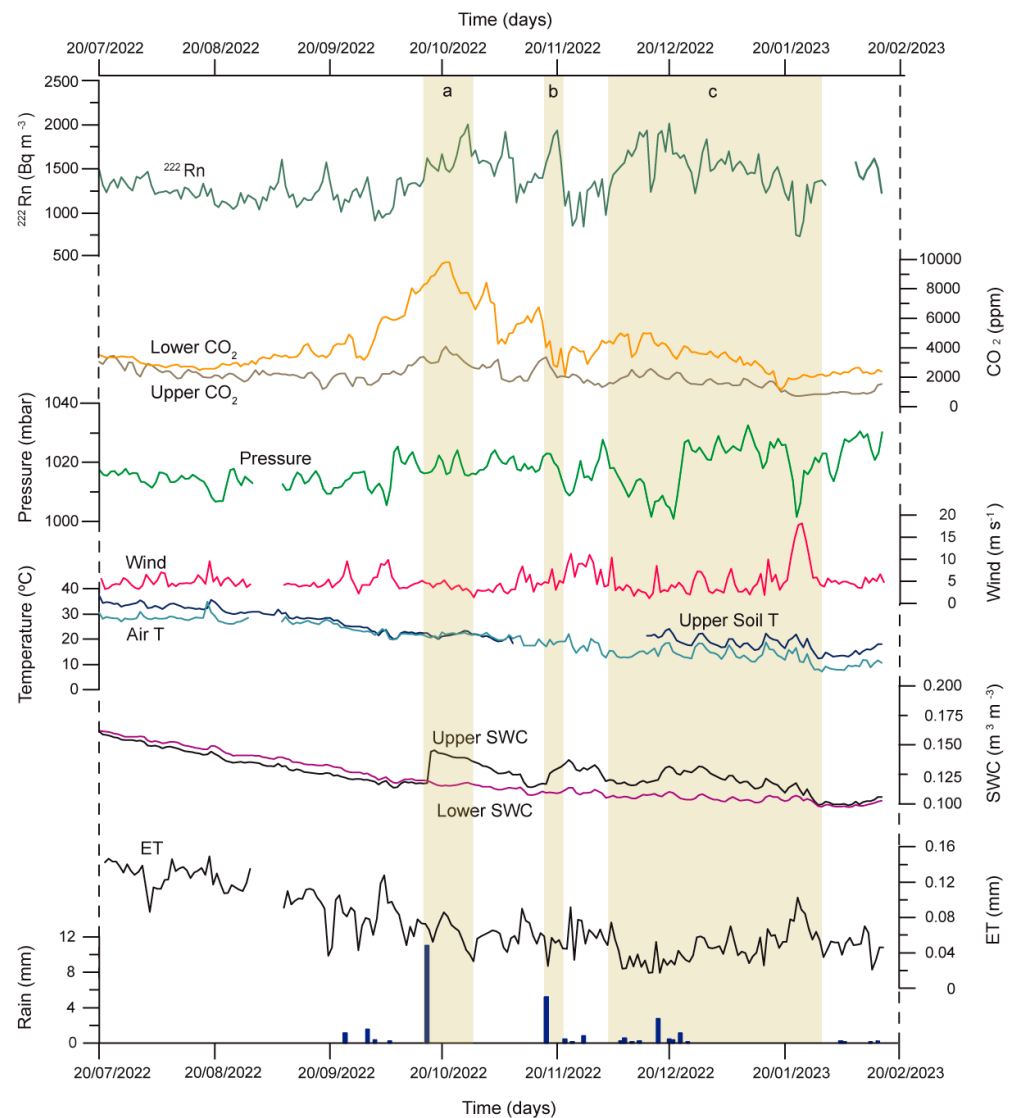


**Figure 3.** Daily temporal evolution of soil and weather variables in calcareous soil for the period July 2022–February 2023. The measured variables from bottom to top are as follows: rain (mm); ET (mm); continuous records of SWC in the upper and lower layers of the soil column ( $\text{m}^3 \text{m}^{-3}$ ); continuous records of Air T and Soil T at the upper and lower layers of the soil column ( $^{\circ}\text{C}$ ); continuous record of Wind ( $\text{m s}^{-1}$ ); continuous record of P (mbar); continuous records of  $\text{CO}_2$  concentration at the upper and lower layers of the soil column (ppm); and continuous  $^{222}\text{Rn}$  activity at the lower layer ( $\text{Bq m}^{-3}$ ). The remarkable periods discussed in the text are highlighted in yellow, labelled as a, b, and c.

### 3.1.1. Granite Soil

The mean value of radon was  $4215 \pm 960 \text{ Bq m}^{-3}$  (Figure 2). Radon activity was generally below this average in the dry season (mainly summer) and usually higher than this value in the rest of the seasons. Radon was close to its maximum with multiple peaks due to radon oscillations often related to rain (Figure 2 (e)). The average concentration of  $\text{CO}_2$  was  $5414 \pm 2284 \text{ ppm}$  and  $4502 \pm 2462 \text{ ppm}$  (upper and lower layer, respectively; Figure 2), and its highest concentration also corresponds to the rainy periods (mainly spring) with a maximum concentration of  $28,994 \pm 423 \text{ ppm}$  (discrete sampling). The mean soil temperature was  $19.3 \text{ }^{\circ}\text{C}$  (Figure 2), and it showed diurnal and seasonal patterns. Soil temperature undergoes a large-scale tendency to increase from the end of winter onwards, reaching the highest temperatures in summer, and then gradually decreasing until winter ( $38.5 \text{ }^{\circ}\text{C}$  and  $2.8 \text{ }^{\circ}\text{C}$ , respectively). The most significant diurnal temperature contrast occurs during the winter–spring months (Figure 2). The mean soil water content was  $0.074 \text{ m}^3 \text{m}^{-3}$



and  $0.058 \text{ m}^3 \text{ m}^{-3}$  (upper and lower layer, respectively; Figure 2). The gas permeability of the granite soil has a typical value of  $10^{-10.63} \text{ m}^2$  ( $\text{pk}_g = 10.63$ ; where  $\text{pk}_g = -\log k_g (\text{m}^2)$ ) measured at  $\text{SWC} = 0.058 \text{ m}^3 \text{ m}^{-3}$ . It can be classified as very permeable according to Neznal et al. [7].

### 3.1.2. Calcareous Soil

Compared to the granite soil, the variation in radon in calcareous soil over time was slightly less sensitive to changes. The mean radon activity was  $1363 \pm 814 \text{ Bq m}^{-3}$  (Figure 3), and its activity was also strongly dependent on the soil water content. The  $\text{CO}_2$  soil concentration has a mean value of  $1471 \pm 485 \text{ ppm}$  and  $2328 \pm 415 \text{ ppm}$  (upper and lower, respectively; Figure 3), and presents lower continuous values than granite soil. The average soil temperature was  $20.6 \text{ }^\circ\text{C}$ , with the highest and lowest values in summer and winter ( $39.5 \text{ }^\circ\text{C}$  and  $3.4 \text{ }^\circ\text{C}$ , respectively). The mean soil water content (SWC) was  $0.126 \text{ m}^3 \text{ m}^{-3}$  and  $0.120 \text{ m}^3 \text{ m}^{-3}$  (upper and lower measurements, respectively; Figure 3). The percentage of sand, silt, and clay (% SSC) in the calcareous soil behaves differently than in the granite soil, and consequently, the calcareous topsoil experienced considerably less variation after rain episodes (Figure 3 (a); October 2022). For an SWC value of  $0.101 \text{ m}^3 \text{ m}^{-3}$ , the calcareous soil was less gas-permeable ( $\text{pk}_g = 10.79$ ) than granite due to its fine texture and larger SWC.

### 3.2. Influence of Weather and Soil Parameters on Radon Dynamics

The impact of weather factors on radon was obtained from the analysis of continuous time series (Figures 2 and 3). In granite soil, the series began during the early spring rains of 2021, which resulted in elevated radon activity (above the mean  $4215 \text{ Bq m}^{-3}$ ) concurrent with the maximum  $\text{CO}_2$  (Figure 2 (a)). Fluctuations in surface soil water content (SWC), mostly below the average ( $0.074 \text{ m}^3 \text{ m}^{-3}$ ), showed discrete peaks at the end of May 2021 (Figure 2 (b)), aligning with a significant rainfall episode. Thereafter, radon activity decreased in late summer, coinciding with a reduction in precipitation and an increase in temperature (Figure 2). In autumn, radon peaks increased during rainy periods. Upper-layer SWC values rose with autumn rainfall, along with the highest radon peaks (Figure 2 (c)). Wind gusts from late autumn 2021 until early winter 2022, without rain episodes, are related to radon fluctuations (Figure 2 (d)). Radon stabilised above the mean after January 2022. March 2022 rains led to a substantial increase in upper-layer SWC, while values in the lower layer remained unchanged (Figure 2 (e)). Radon and SWC increased, reaching their highest levels in April and May 2022. The radon peak in May 2022 coincided with the second-highest rainfall event, leading to a notable increase in  $\text{CO}_2$  (Figure 2 (e)). At the beginning of June 2022, radon decreased again, in conjunction with a decrease in  $\text{CO}_2$  and soil moisture, while temperatures rose.

As observed in the granite soil, from July 2022 to the beginning of January 2023, temperature and SWC in the calcareous soil gradually decreased in the seasonal trend while the radon increased (Figure 3). SWC was affected by the most important rainfall event of the series (Figure 3 (a)). Rain events during mid- and late-autumn 2022 caused a notable impact on radon activity, particularly following two significant rainfall episodes in October and November 2022 (Figure 3 (a,b)). Then, the wind gusts coincided with a decline in radon. Additionally, the late autumn period (Figure 3 (c), concluding the December 2022 rain events) showed a low-pressure trend, aligning with a slight increase in radon activity. In winter 2022, strong wind gusts were recorded along with a decrease in radon activity (Figure 3 (c)).

The two continuous soil series clearly show how the weather variables influence radon dynamics, especially in granite soil. Both SWC and temperature were identified as conditioning variables, and SWC was the parameter likely to exert the most significant influence on radon activity [43,60]. The water content is also analysed in Section 3.3. High temperatures in summer (i.e., also higher ET) are seasonally associated with low SWC values and low radon activity [61,62].

In fact, the response of the radon variations to the SWC depends on the initial SWC in each seasonal period. Therefore, for a semi-arid climate such as Alicante, radon activity generally increases more with longer periods of rainfall events (Figure 2 (e)). Thus, maximum values of radon peaks occurred during periods of high soil moisture linked to rainfall, as Pinault et al. [63], Tareen et al. [64], and Naskar et al. [65] described. In the calcareous soil, the occurrence of maximum values of radon peaks following rainfall events was delayed when compared to the granite soil, likely due to its loamy and clayey texture (Table 1).

Both soils exhibit different responses to rainfall events related to SWC variations closer to the surface and deeper layers. Close to the soil surface, SWC achieved higher and more variable values, compared to the more stable SWC in the lower layer, less influenced by weather conditions [30,31]. In the case of calcareous soil, the SWC of the deeper layer was less affected and remained nearly constant after rainfall events, which lasted from a few hours to days until the water reached a peak in the lower SWC layer. This was particularly evident during continuous rainfall periods (Figure 2 (e)).

The increase in water in the upper soil layer reduces soil gas permeability. Consequently, radon activity rises in the lower soil layer due to the combined effects of recoil and the gas being trapped in the soil under a water-saturated layer [12], which reduces gas transport [14,26,66–68].

CO<sub>2</sub> fluctuations also respond to SWC variations, similar to radon, and although radon and CO<sub>2</sub> have different sources, they are commonly used as tracer gases in various geoscience disciplines [38,39]. In our context, the concentration of CO<sub>2</sub> is linked to microbiological activity and is dependent on water content and temperature [69,70]. Both CO<sub>2</sub> and radon increased with SWC, mainly in spring and autumn (Figures 2 (c,d) and 3 (a)). They also share a similar downward trend at the end of spring and during the summer period (Figure 2 (e)), regarding an increase in soil temperature and evapotranspiration, and a drop in microbiological activity (in case of CO<sub>2</sub>).

Barometric pressure and high wind velocities can influence radon activity, although their impact is generally considered less significant. They have a more pronounced impact on radon activity in highly permeable soils [12]. However, in the current time series, SWC variations related to rain events do not allow a proper visual evaluation of their influence on radon activity changes. Large-scale barometric pressure changes and high wind velocities correlated inversely with radon activity (Figures 2(d) and 3 (c)). The decrease in barometric pressure draws soil air to the surface, affecting the radon activity in deeper soil layers. Similarly, high wind velocities locally depressurise, and radon activity decreases [35].

### 3.3. Artificial Soil Water Content Experiment

The results obtained in the previous analyses highlighted the relevance of water content on soil radon activity in the studied soils. For this reason, we forced soil water conditions with an experiment that was developed to better understand the relationship between soil water content and soil radon variations.

In granite soil, soil temperature showed natural daily temperature variations, while the SWC changes were entirely consequences of the artificial addition of water (Figure 4). Water content was first detected at the upper sensor 2 min after the first water addition. It flowed downwards by water infiltration, and it was detected in the lower measurement point 4.03 h after the first water addition. The different SWC peaks (0.230, 0.230, and 0.246 m<sup>3</sup> m<sup>-3</sup> in the upper layer; 0.144 and 0.145 m<sup>3</sup> m<sup>-3</sup> in the lower layer; Figure 4) are a consequence of the different water additions. As the soil becomes saturated, the water infiltration is constant from the upper to the lower point of the soil column.

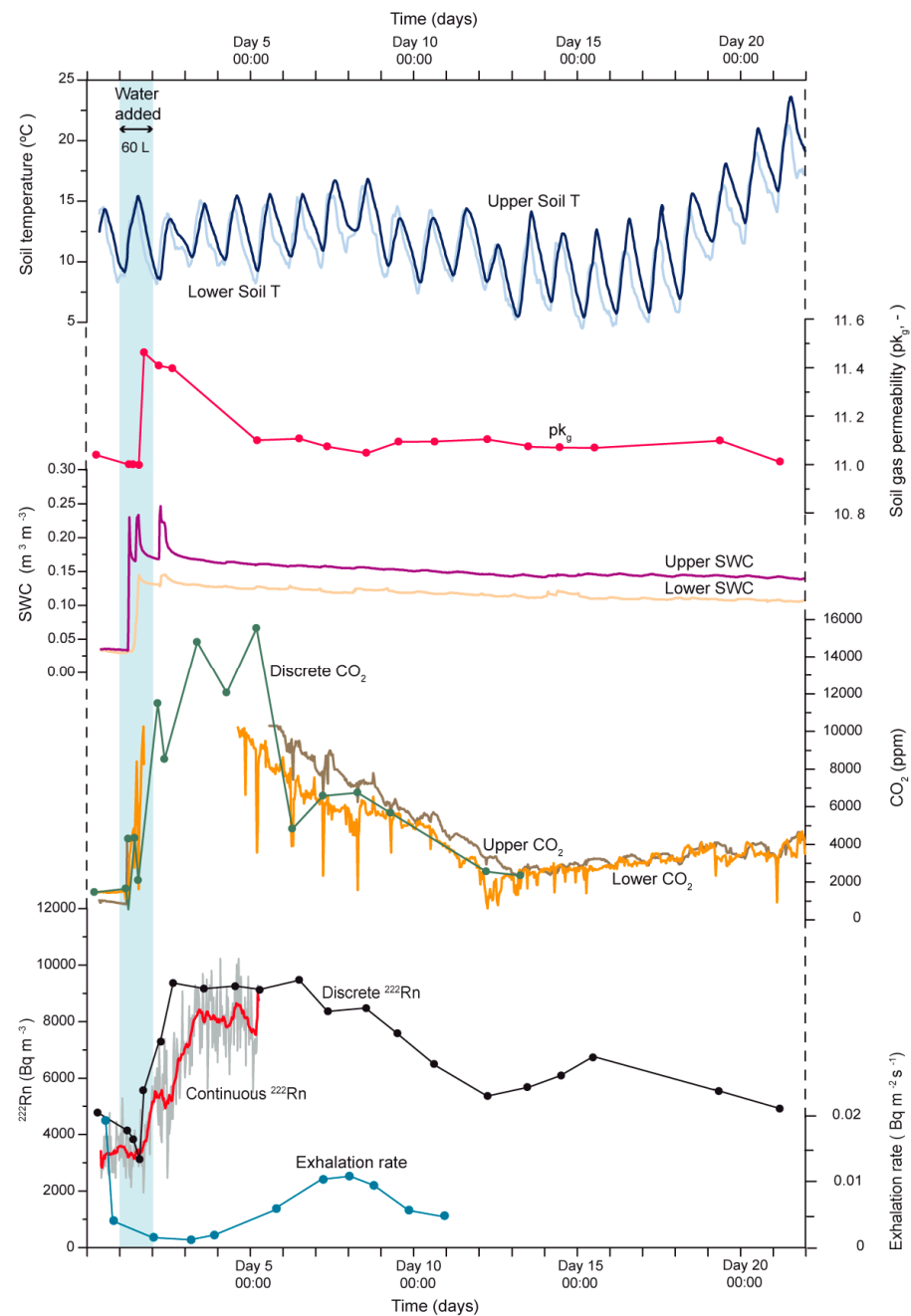


**Figure 4.** Evolution of soil and weather variables in the artificial soil water content (SWC) experiment of the granite soil. The measured variables from bottom to top are as follows: radon exhalation rate ( $Bq m^{-2} s^{-1}$ ); discrete, continuous, and smooth continuous records of  $^{222}Rn$  activity in the lower soil column layer ( $Bq m^{-3}$ ); discrete and continuous records of  $CO_2$  concentration at the upper and lower layers of the soil column (ppm); continuous records of SWC at the upper and lower layers of the soil column ( $m^3 m^{-3}$ ); soil gas permeability, in  $pk_g$  terms, at the lower layer of the soil column (-); and continuous records of the Soil T at the upper and lower layers of the soil column ( $^{\circ}C$ ). The period of water addition is highlighted in blue.

Radon activity at the beginning of the experiment ( $3301 Bq m^{-3}$ ) was below the average measured in continuous monitoring ( $4215 Bq m^{-3}$ ; Figure 2). With the addition of water, radon activity sharply increased, reaching up to  $9170 Bq m^{-3}$  (Figure 4). This increase occurred in a period ranging from 14 to 22 h from the beginning of the experiment. Afterwards, radon activity remained stable for approximately 4 days, from which it decreased and returned closer to its initial values ( $2266 Bq m^{-3}$ ). After the fifth day

of the experiment, the continuous measurement of radon was replaced by discrete daily measurements (Figure 4) that confirmed the reduction in its activity over time. Concerning CO<sub>2</sub>, a similar pattern is described, with an increasing concentration in response to the addition of water to the soil. Both gases reached maximum values as a fast response to water addition and showed a drop nearly four days after the beginning. Maximum concentrations of CO<sub>2</sub> (greater than 14,000 ppm) were not measured by the continuous probes but by taking discrete samples.

The radon exhalation rate shows a decrease with respect to the value measured before the addition of water (first measurement of the series; Figure 4). As the soil porous network was filled with water, radon could not migrate through the soil pores towards the atmosphere. Consequently, exhalation values recorded on the soil surface are the lowest with maximum water contents.

Before conducting the artificial soil water content experiment,  $pk_g$  was 11.00 ( $k_g = 10^{-11.00} \text{ m}^2$  is considered high gas permeability according to Neznal et al. [7]). After the second water addition, soil gas permeability decreased to its minimum ( $pk_g = 11.46$ ). This coincided with the growth of radon activity and its highest recorded level. Gas permeability has a clear variation throughout the experiment (from  $10^{-11.00}$  to  $10^{-11.46} \text{ m}^2$ ). In addition, there was a notable difference in soil temperature between the beginning and the end of the experiment, considering both minimum and maximum (maximums began around 15 °C, while at the end, they were close to 25 °C; Figure 4). This was accompanied by a decrease in radon activity, which was in concordance with the soil drying process and the removal of water from the pore space, allowing the migration of radon outwards.

Figure 5 shows the artificial soil water condition experiment performed in the calcareous soil, which displays different soil variable dynamics compared to the granite soil, especially regarding radon. Soil temperature was also influenced by the daily air temperature oscillations and the gradual warming trend. Water added to this soil was less than that in the granite due to significantly reduced vertical infiltration through the soil column, related to its field capacity. Consequently, water remained stagnant on the soil surface, causing ponding. This caused all calcareous soil variables to evolve more slowly.

Water infiltration was detected in the upper sensor 4 min after the first water addition, while the detection in the lower sensor occurred 2 days and 2.2 h later. Thus, the maximum SWC in the bottom layer (nearly  $0.20 \text{ m}^3 \text{ m}^{-3}$ ) was lower compared to the upper soil layer (nearly  $0.30 \text{ m}^3 \text{ m}^{-3}$ ; Figure 5). However, the variation in SWC in the lower layer did not cause a change in gas permeability, as with granite ( $pk_g$  remained nearly constant at 10.73).

Radon activity shows two pulses: one during the period of water addition and another just after this period. In the first one, radon activity increased progressively until it reached a peak on day 5 ( $3930 \text{ Bq m}^{-3}$ ; Figure 5), then decreased and returned to values similar to the beginning. The second pulse recorded a similar trend but with slightly higher activities, reaching an overall maximum on day 13 ( $5292 \text{ Bq m}^{-3}$ ; Figure 5). Between days 13 and 14, the maximum activities occurred, and then radon decreased and began more pronounced fluctuations.

The latter coincides with a barely perceptible decrease in the Upper SWC, while the Lower SWC remains constant at a value that shows a double contrast to that at the beginning. This in turn coincides with the increase in temperature.

Radon exhalation rates were lower compared to the granite soil, even slightly lower after starting the experiment because of stagnant surface water, as well as the radium content and the water retention related to its texture. Finally, regarding CO<sub>2</sub> concentration, it gradually increased until the highest radon activity was reached (day 13). From then on, CO<sub>2</sub> showed similar dynamics to radon but with a larger amplitude between peaks and drops. It reached its maximum recorded level 21 days after the beginning of the experiment.

The experiments showed that there was more water than air in the pore system, mainly in the upper layer. This increases radon emanation [71]. When the water content is very high, gas permeability decreases and radon is diluted in water, resulting in no soil-atmosphere exchange (radon exhalation rate decreases). In lower layers, radon activity

increases until the upper layer is no longer saturated as the soil dries out, favoured by rising temperatures. It is at this point that the gas permeability increases (increased exhalation rate [72]), and radon activity decreases due to exchange with the atmosphere. In the case of calcareous soil, the process is more complex, conditioned by a lower content of sand-sized particles and a higher percentage of silt and clay.

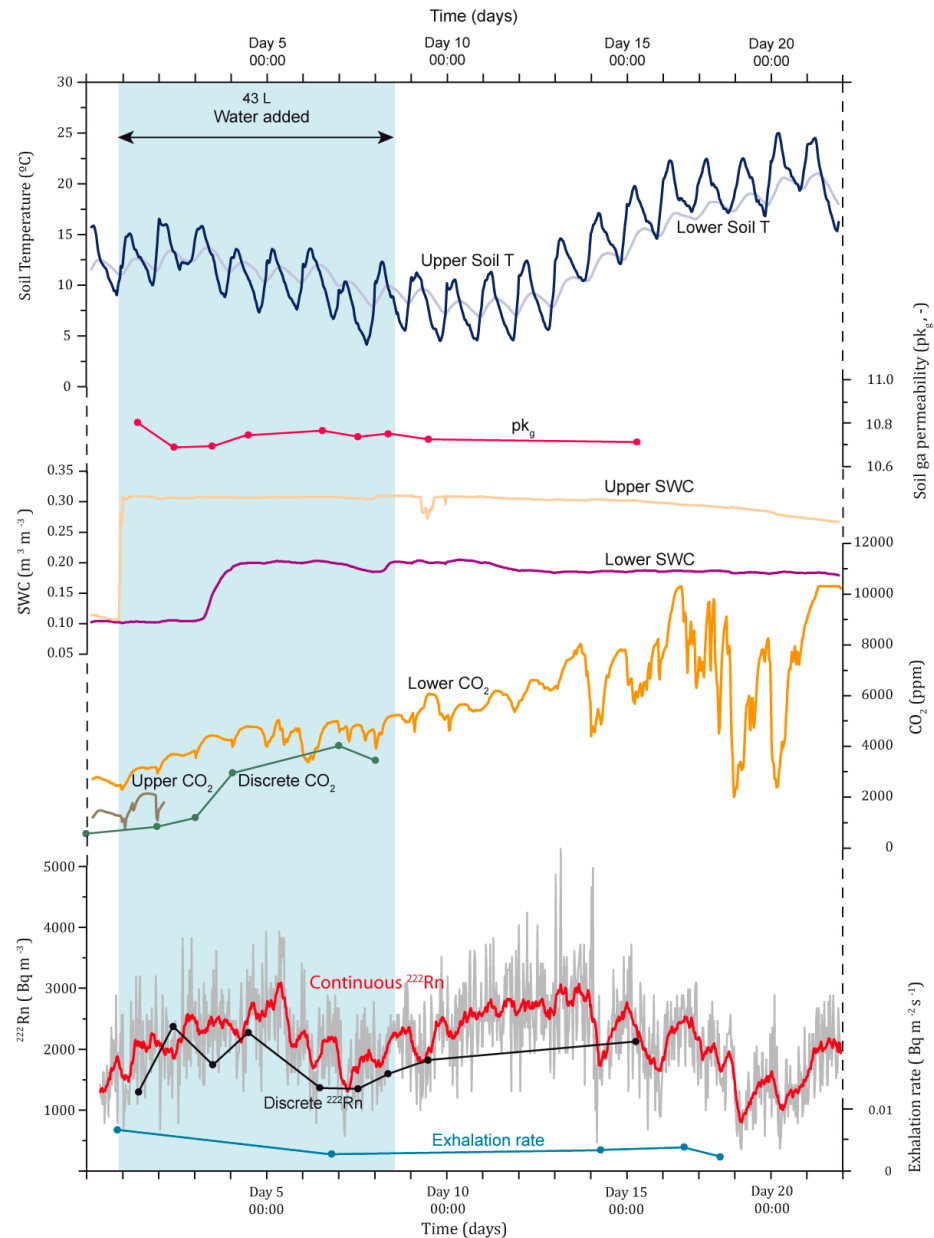


**Figure 5.** Evolution of soil and weather variables in the artificial SWC experiment of the calcareous soil. The measured variables from bottom to top are as follows: radon exhalation rate ( $\text{Bq m}^{-2} \text{s}^{-1}$ ); discrete, continuous, and smooth continuous records of  $^{222}\text{Rn}$  activity in the lower soil column layer ( $\text{Bq m}^{-3}$ ); discrete and continuous records of  $\text{CO}_2$  concentration at the upper and lower layers of the soil column (ppm); continuous records of SWC at the upper and lower layers of the soil column ( $\text{m}^3 \text{m}^{-3}$ ); soil gas permeability, in  $\text{pk}_g$  terms, at the lower layer of the soil column (-); and continuous records of the Soil T at the upper and lower layers of the soil column ( $^\circ\text{C}$ ). The period of water addition is highlighted in blue.

#### 4. Discussion

This section aims to discuss the data recorded from both soil time series in order to understand the processes and variables affecting radon dynamics. First, the statistical determination of the relationship between radon variability and the other variables is addressed. According to the results obtained, the granite soil was initially selected to study discrete rain events with significant variations in radon because its texture allowed us to obtain clearer evidence of changes in radon and the other variables. Based on this analysis, we conducted a global analysis of the time series for both soils at daily intervals. Additionally, the long-term radon activity pattern was characterised using wavelet analyses to evaluate the interrelations between pairs of variables. Finally, based on our results, we evaluated and estimated radon potential estimation related to radon response to weather parameters and soil properties.

##### 4.1. Time Series Analyses

##### 4.1.1. Statistical Analyses of the Granite Soil

This analysis considered the detection of discrete events with significant variations in radon activity related to rainfall episodes. The main variables associated with these events are initial radon activity ( $Rn_0$ ), maximum radon reached after the rain episode ( $Rn_{max}$ ), soil water content in the upper soil layer at  $Rn_{max}$  (Upper  $SWC_{Rn_{max}}$ ), pressure at  $Rn_{max}$  ( $P_{Rn_{max}}$ ), soil temperature at  $Rn_{max}$  (Soil  $T_{Rn_{max}}$ ), wind speed at  $Rn_{max}$  ( $Wind_{Rn_{max}}$ ), and accumulated rainfall (Rain).

The principal component analysis (PCA) of these variables defined two principal components (PCs), which accounted for 62.3% of the total variance (Table 2). PC1 links  $Rn_{max}$  with initial  $Rn_0$ , and Rain with Upper  $SWC_{Rn_{max}}$ . Thus, the  $Rn_{max}$  reached after the rain episode depends on the initial radon activity before the rain event. As described previously in Section 3.2, rain mainly defines SWC in the upper soil layer and is the weather factor that affects the most radon variations. PC2 associates weather parameters  $Wind_{Rn_{max}}$ ,  $P_{Rn_{max}}$  and Soil  $T_{Rn_{max}}$  (similar to air temperature pattern), and they act differently when radon reaches its maximum after the rain episode.

**Table 2.** Principal component analysis (PCA) and multiple linear regression (MLR) of discrete events with significant variations in radon related to each rainfall episode in the granite soil. PC corresponds to principal components in the PCA. B and Beta are the coefficients and the standardised coefficients of the MLR, respectively, with their associated *p*-value. Significant codes: *p*-value: 0.05 ‘\*’; >0.1 ‘-’.  $Rn_{max}$  acts as the dependent variable.

Variables	Principal Component Analysis		Multiple Linear Regression		
	PC1	PC2	B	Beta	<i>p</i> -Value
$Rn_{max}$	0.871	−0.007	65,674.43		*
Rain	0.654	0.225	77.94	0.31	*
$Rn_0$	0.702	−0.274	0.34	0.33	*
Upper $SWC_{Rn_{max}}$		0.161	−515.95	−0.03	-
$P_{Rn_{max}}$	−0.399	−0.652	−58.84	−0.35	*
$Wind_{Rn_{max}}$	0.024	0.780	60.63	0.14	-
Soil $T_{Rn_{max}}$	−0.456	0.754	−88.78	−0.43	*

Multiple linear regression (MLR) analysis aims to evaluate the significant weight of each variable (acting as independent variables) on the estimation of the maximum radon reached after the rain episode (acting as the dependent variable). In other words, it is a qualitative approach to evaluate which variable affects  $Rn_{max}$  the most, rather than providing a predictive equation. The combination of all the variables considered (Table 2) to estimate  $Rn_{max}$  leads to an excellent goodness-of-fit, with Pearson’s coefficient, R, being 0.816. In the MLR,  $Rn_0$ ,  $P_{Rn_{max}}$  and Soil  $T_{Rn_{max}}$  can be considered significant variables in the estimation of  $Rn_{max}$  (Table 2). This analysis focuses on the variation in radon related

to each rainfall episode in granite soil, where  $Wind_{Rn\ max}$  does not significantly influence  $Rn_{max}$  dynamics.

Based on these results related to rainfall episodes, we analysed the entire time series at a daily frequency. The dataset contains the following variables: radon activity (Rn), soil water content in the upper soil layer (Upper SWC), soil temperature (Soil T), wind speed (Wind), and pressure (P). Moreover, here, we considered evapotranspiration (ET). Rain was excluded from these analyses because it was discrete throughout the entire time series. Instead, SWC, which represents rainfall effect on soil, was evaluated.

In this case, PCA results in three components that explain 85.6% of the variance and show that Rn was found in two principal components (Table 3), PC1 and PC2. In PC1, Rn was inversely related to Soil T and ET, whereas it was positively related to barometric pressure. As ET increases, SWC decreases, causing radon to migrate from the soil into the atmosphere. Conversely, an increase in P retains soil air in the lower soil layer. In PC2, radon (Rn) was positively related to Upper SWC and inversely related to P, highlighting the importance of SWC in the accumulation of radon at the lower layer. PC3 only includes Wind and it was not directly related to Rn.

**Table 3.** PCA and MLR of entire time series at a daily frequency in the granite soil. PC corresponds to principal components in the PCA. B and Beta are the coefficients and the standardised coefficients of the MLR, respectively, with their associated *p*-value. Significant code: *p*-value: 0 '\*\*\*\*'. Rn acts as the dependent variable.

Variables	Principal Component Analysis			Multiple Linear Regression		
	PC1	PC2	PC3	B	Beta	<i>p</i> -Value
Rn	−0.639	0.613	0.379	22,690.39		****
Upper SWC	−0.329	0.890	−0.050	9834.87	0.60	****
Soil T	0.886	0.063	0.401	−53.09	−0.57	****
Wind	0.249	0.245	−0.911	−173.26	−0.57	****
P	−0.580	−0.532	0.100	−17.35	−0.13	****
ET	0.795	0.325	0.196	5210.02	0.25	****

The MLR analysis found that all variables are significant, considering the daily dataset (Table 3). Pearson's coefficient is 0.859, and it considers Upper SWC, Soil T, and Wind to have the most statistical weight in the model (higher standardised coefficients—Beta values). Despite PCA concluding that Rn and Wind act differently, the MLR analysis highlights that Wind was a weather parameter that must be considered on a long-term scale in these soils and the climate context.

Different studies have demonstrated that the correlation of radon activity with meteorological variables is complex and does not follow a specific pattern, being dependent on the study site [72–74]. Regarding similarities with this granite soil, Papachristodoulou et al. [45] and Tareen et al. [64] also described a positive correlation with pressure, and Turk et al. [75] observed a positive correlation with water content in soil.

#### 4.1.2. Statistical Analyses of the Calcareous Soil

The PCA of the calcareous soil explains 67.1% of the variance, described by two principal components (Table 4). Rn was included in PC1, although its loading coefficient was low (−0.499). In other words, it is not well described in PC1, which hinders the correlation with other variables. Therefore, Rn is positively correlated with P (although it has a low loading coefficient, like in the granite soil) and inversely correlated to Upper SWC, Soil T, and ET. PC2 only contains the Wind variable.

**Table 4.** PCA and MLR of the entire time series at a daily frequency in the calcareous soil. PC corresponds to principal components in the PCA. B and Beta are the coefficients and the standardised coefficients of the MLR, respectively, with their associated *p*-value. Significant codes: *p*-value: 0 '\*\*\*\*'; 0.01 '\*\*'; >0.1 '-'. Rn acts as the dependent variable.

Variables	Principal Component Analysis		Multiple Linear Regression		
	PC1	PC2	B	Beta	<i>p</i> -Value
Rn	−0.499	0.320	−12,020.20		****
Upper SWC	0.790	0.397	3982.40	0.19	-
Soil T	0.929	0.229	−4.19	−0.13	-
Wind	0.096	−0.830	9.94	0.10	-
P	−0.537	0.489	12.86	0.29	**
ET	0.867	−0.028	−2128.16	−0.28	-

MLR analysis reveals a low linear correlation between the variables studied, as Pearson's coefficient for the MLR is 0.442. Most of the variables have low statistical weight in the estimation of radon. However, the sign of the coefficients in the MLR equation (B) clarifies the relationship between Rn and soil and weather parameters. Thus, Rn was positively correlated with Upper SWC, Wind, and P, and negatively correlated with Soil T and ET, which is in agreement with the general trend of the calcareous soil in the time series.

As calcareous soil has a silty clay loam texture, its hydraulic properties and water retention are different from granite (loamy sand soil, Figures 2–5), as demonstrated in both the long-term time series and the experimental rain study. Furthermore, the time series in the calcareous soil is shorter than in the granite soil, and it does not include rainfall events that could affect the SWC comparably to the granite soil. Consequently, these results are not as conclusive as those observed in the granite soil, which emphasises the need for individual analysis of each soil for a better understanding of the radon potential.

#### 4.1.3. Wavelets

For the granite soil, the results of wavelet analyses confirmed the influence of soil water content, soil temperature, evapotranspiration rate, pressure, and wind speed on radon (Figures 6 and 7), also highlighted in the previous analysis.

For the period selected to perform the analysis, important changes in SWC caused a response in radon activity (Figure 7a,b). In the granite soil, rainfalls of November 2021, March–April 2022, and May 2022, which caused an increase in SWC, resulted in an evident increase in radon activity, in all cases occurring simultaneously. Therefore, the individual analysis of both signals established a predominant periodicity from one to several days with the rainfall episodes when they occurred (Figure 7a,b). Within these episodes, SWC and radon activity coincided in the time–frequency domain, showing interrelations explained by cross wavelet transform (XWT) and its wavelet transform coherence (WTC). Furthermore, the effect of pressure and wind variations on radon was also highlighted in the analysis (Figures 6e,f and 7g–j) with marked areas with high common power in the scalograms. These areas are higher in the radon–pressure analysis, indicating a larger influence of these variables [76]. Concerning the influence of soil temperature and ET (Figures 6c,d and 7c–f), the wavelet analysis does not reveal conclusive results, as common areas with strong power (in the case of radon–Soil T or radon–ET) were not detected in the time–frequency domain.

For the calcareous soil, wavelet analysis (Figures 6 and 8) identified areas with high common power between pairs of signals, which might be significant in the case of pressure or wind (Figures 6k,l and 8g–j). For these variables, XWT and WTC identify areas of high common power that coincide with the results of the individual analysis of the different signals (Figure 8e,f) in which the different predominant periodicities are established. The scalogram identifies common behaviours between coincident periodicities that exist for these variables and radon. However, SWC's interrelation with radon (XWT; Figure 8a) is weaker compared to granite soil. It appears continuously for the time range in the 64-day period band, but neither in the WTC (Figure 8b) nor in the individual SWC analysis



(Figure 6a). No significant common power areas are identified for soil temperature and ET (Figures 6i,j and 8c–f).

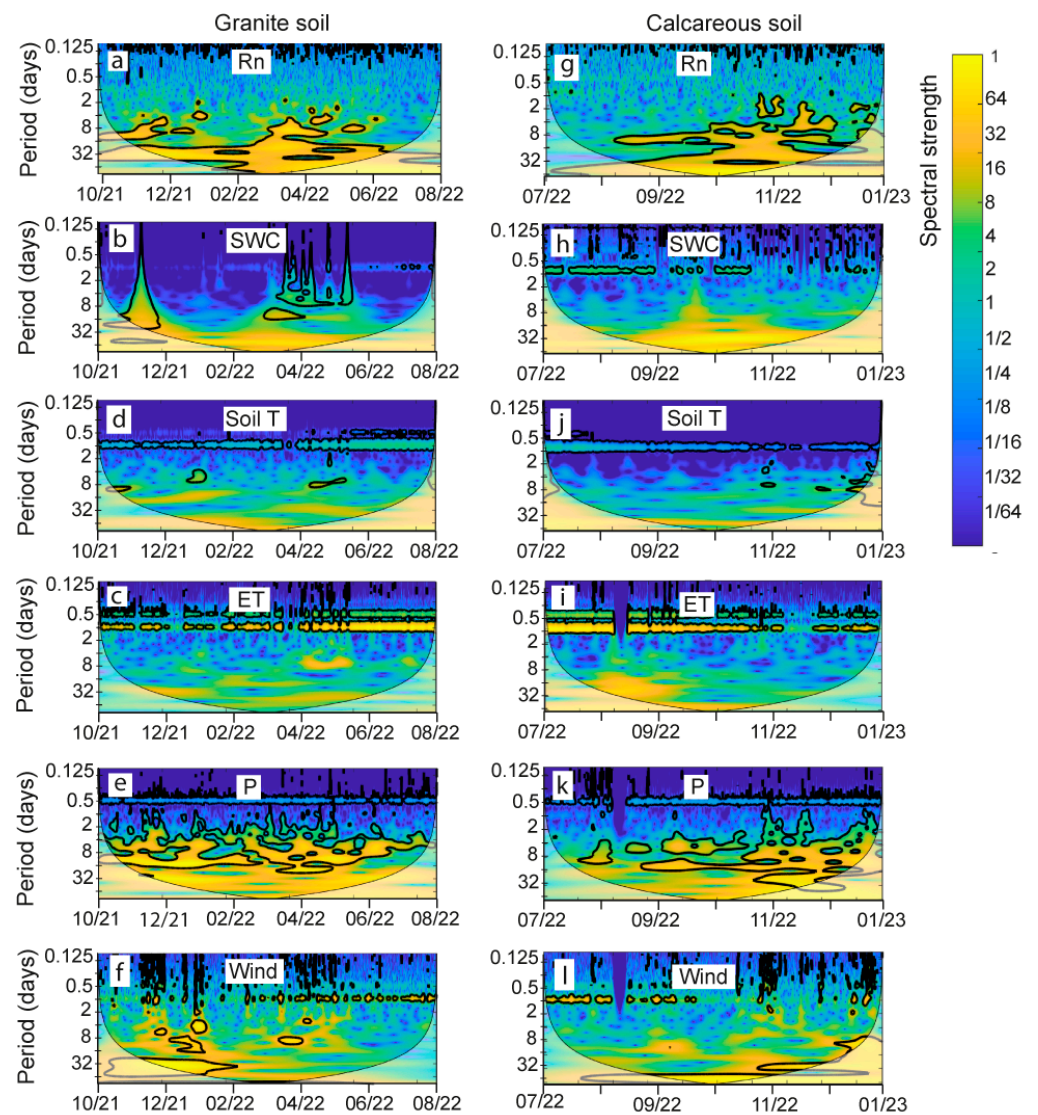


**Figure 6.** Decomposition of the different periodicities for radon (Rn; (a,g)), soil water content (SWC; (b,h)), soil temperature (Soil T; (c,i)), evapotranspiration (ET; (d,j)), pressure (P; (e,k)), and Wind (f,l) of the granite and calcareous soils; spectral strength and coherence range from blue (weak) to yellow (strong) colours.

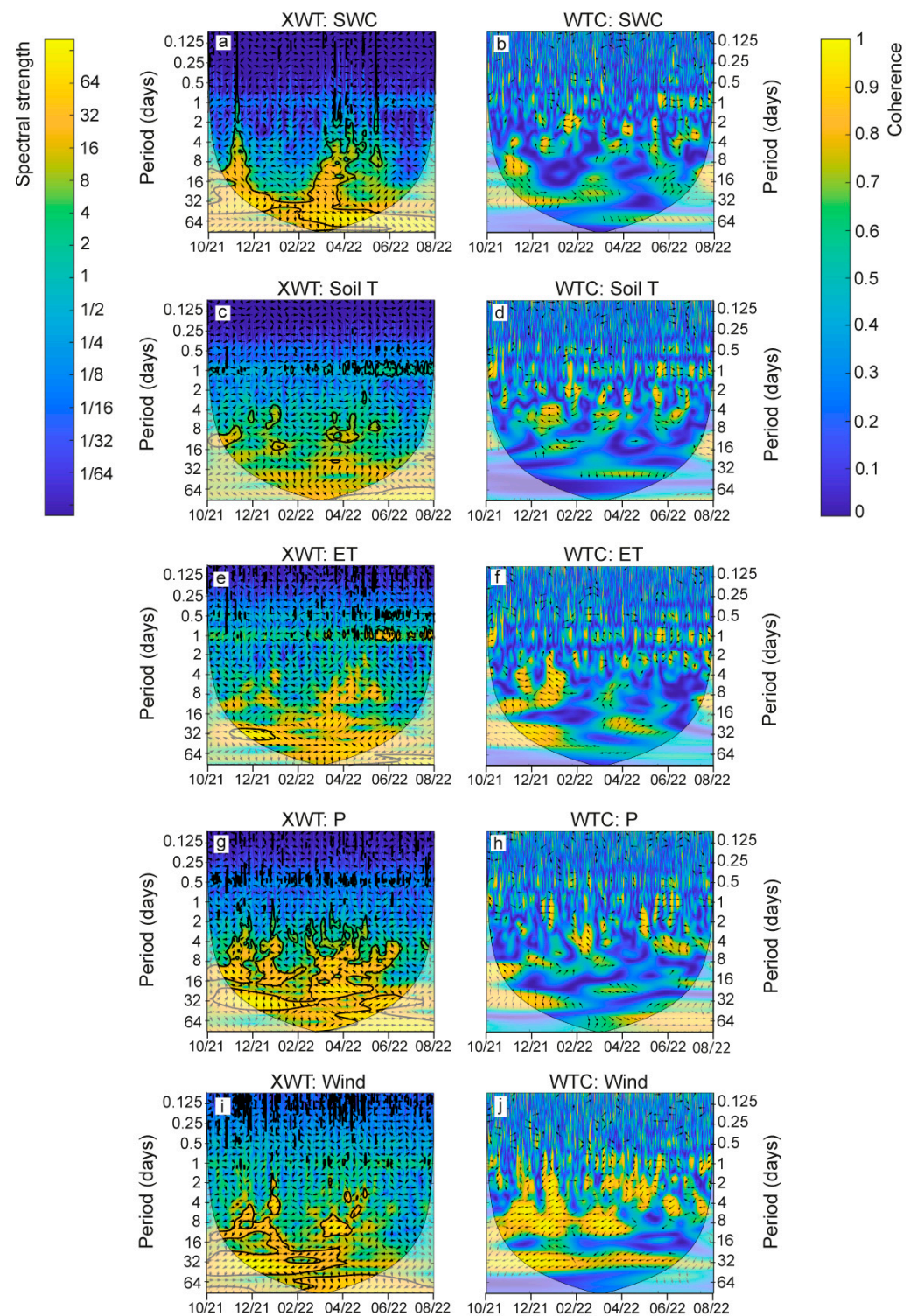


**Figure 7.** WTC and XWT of the granite soil between  $^{222}\text{Rn}$  and SWC (a,b), Soil T (c,d), ET (e,f), P (g,h), and Wind (i,j); spectral strength and coherence range from blue (weak) to yellow (strong) colours. Arrows indicate the relative phase relationship (in phase pointing right, antiphase pointing left, one signal leading the other by  $90^\circ$  pointing up/down). Curved lines on scalograms indicate the cone of influence where the edge effects are important.

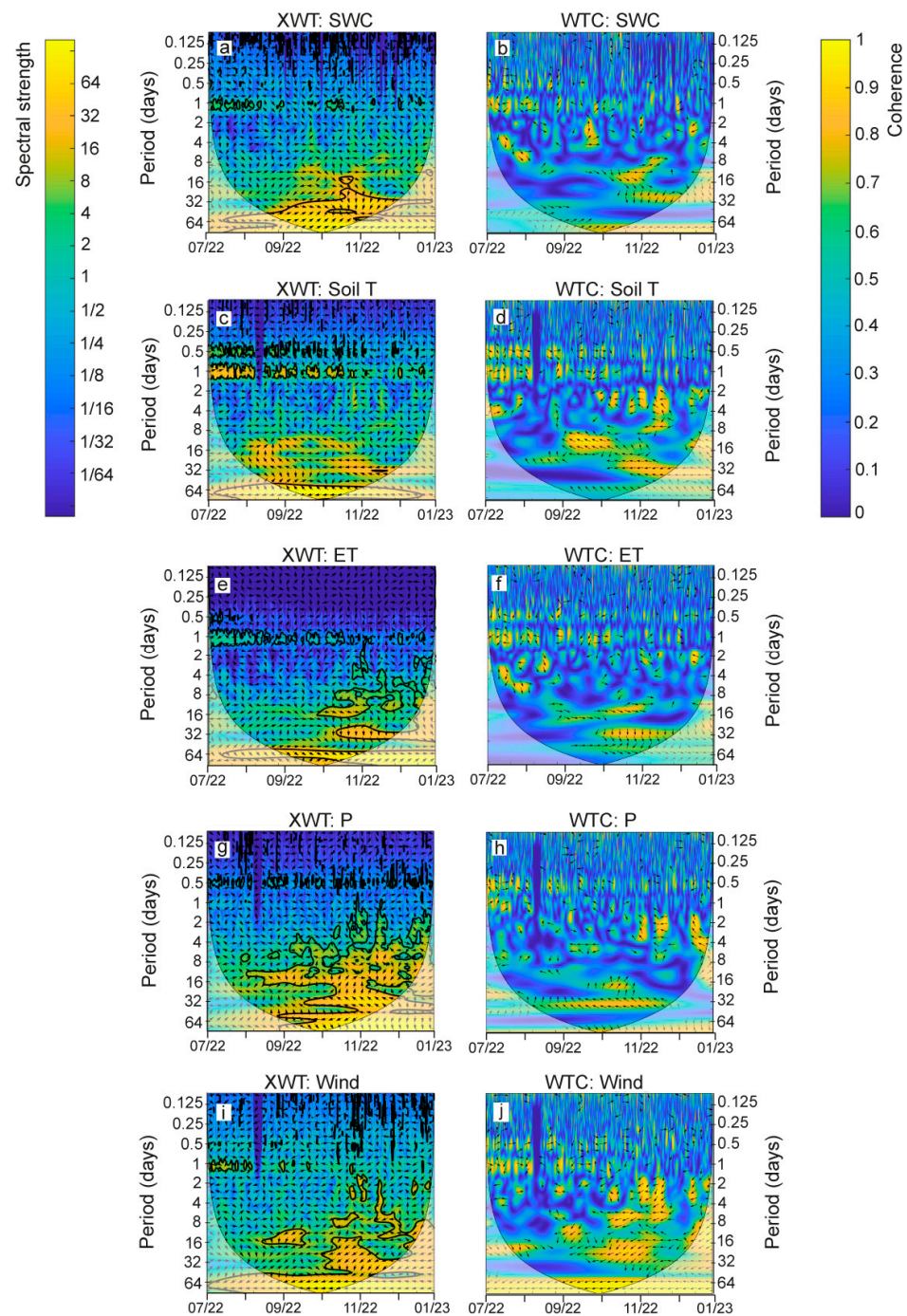


**Figure 8.** WTC and XWT of the calcareous soil between  $^{222}\text{Rn}$  and SWC (a,b), Soil T (c,d), ET (e,f), P (g,h), and Wind (i,j); spectral strength and coherence range from blue (weak) to yellow (strong) colours. Arrows indicate the relative phase relationship (in phase pointing right, antiphase pointing left, one signal leading the other by  $90^\circ$  pointing up/down). Curved lines on scalograms indicate the cone of influence where the edge effects are important.

#### 4.2. Radon Potential

The detailed analysis of long-term time series has demonstrated that radon dynamics are largely determined by weather parameters and soil properties, and their interactions. Soil water content (SWC) was the parameter likely to exert the most significant influence on radon in soil air. However, its response to rainfall events and variability within the soil depth depends on the type of soil. Barometric pressure, temperature, and wind also affect radon soil activity, although their impact was less significant.

Thus, processes that alter radon activity and its mobility in the soil have an impact on the radon hazard assessment. As previously introduced, the geogenic radon potential can be considered an indicator of radon activity hazard, since radon gas exhalating from the soil is the main contributor to indoor environmental accumulation. It conceptualises ‘what Earth delivers in terms of radon’ from geogenic sources—e.g., radionuclides in soils, rocks, and fractures—to the atmosphere [9,77]. The widely used Neznal equation for the radon potential of a building site (Equation (1) [7]) includes soil gas permeability and radon activity, and it leads to a radon index class. Therefore, soils with high radium and uranium content and high permeability present high RP values, implying a higher probability of indoor radon infiltration due to geological factors. RP can be classified as low ( $RP < 10$ ), medium ( $10 \leq RP < 35$ ), and high ( $RP \geq 35$ ), according to the Neznal et al. [7] classification.

The soils studied are classified as low risk, due to the relatively low concentrations of radium and uranium (Table 1). Initially, we chose granite soil, because it belongs to a radon-prone area, to compare it with the local calcareous soil. However, the radon activity recorded in the long-term series, the gas permeability, and the warm semi-arid climate define this soil as low risk. Consequently, the RP assessment could not be performed properly. Nevertheless, our findings on radon dynamics and their response to changes in the environment and soil properties can be used to parametrise and model RP variations. Soil water content and soil texture are quantitatively related to radon activity and gas permeability, and therefore to radon potential.

Radon activity can be estimated from radium activity, since  $^{222}\text{Rn}$  is the  $^{226}\text{Ra}$  decay product. Therefore, the theoretical radon activity can be obtained by the following consolidated expression (Equation (4))—e.g., Åkerblom [78], Giustini et al. [79], and Voltaggio et al. [80]:

$$C_{Rn} = C_{Ra} \cdot \varepsilon \cdot \rho_b, \quad (4)$$

where  $C_{Ra}$  ( $\text{Bq kg}^{-1}$ ) is  $^{226}\text{Ra}$  concentration,  $\varepsilon$  is the emanation coefficient (-), and  $\rho_b$  ( $\text{g cm}^{-3}$ ) is the bulk density. The radon emanation coefficient in soil is a function of soil texture, water content, and temperature, and it is obtained from Equation (5) [81,82]:

$$\varepsilon = \varepsilon_0 \cdot [1 + a(1 - \exp(-b \cdot S_w))] \cdot [(1 + c) \cdot T], \quad (5)$$

where  $\varepsilon_0$  is the radon emanation coefficient at 25 °C for dry soil;  $S_w$  is the water saturation (-);  $T$  (°C) is the soil temperature; and  $a$ ,  $b$ , and  $c$  are three parameters fitted that depend on the soil properties (Table 5). If, as a first approximation, the residual (volumetric) water content is considered zero and the saturated (volumetric) water content is equal to the porosity,  $\phi$ , then  $S_w = \text{SWC} / \phi$ . Radon emanation coefficients can be estimated for any type of soil texture considering a weighted sum of % SSC.

**Table 5.** Fitted parameters and  $^{222}\text{Rn}$  emanation coefficient for clay, silt, and sand [82].

Coefficient	Clay	Silt	Sand
$\varepsilon_0$	0.10	0.14	0.18
$a$	1.85	1.73	1.53
$b$	18.8	20.5	21.8
$c$	0.012	0.01	0.011

Table 5 shows the % SSC for typical clay, silt, loam, and sandy soils. For example, according to Equations (4) and (5), sandy soil has a radon activity of  $15.60 \text{ kBq m}^{-3}$ , whereas clay soil has  $9.54 \text{ kBq m}^{-3}$  (for soil with  $\rho_b = 1.7 \text{ g cm}^{-3}$  and  $C_{Ra} = 50 \text{ Bq kg}^{-1}$  at 20 °C). This calculation reveals the strong influence of soil texture on radon activity and how heterogeneities in the soil profile may determine the local radon activity, without considering other crucial aspects such as radon transport and soil hydraulic properties. Furthermore, the influence of temperature on radon activity is negligible compared to soil texture, considering that daily soil temperature variations at a 100 cm depth are less than

3 °C (Figures 2–5). For example, a change from 20 to 30 °C reduces radon activity from 15.49 to 16.87 kBq m<sup>-3</sup> (for  $C_{Ra} = 50$  Bq kg<sup>-1</sup> and a loam soil defined in Table 6).

**Table 6.** Percentage of sand, silt, and clay (% SSC), and its related  $n$  and  $pk_g$  values according to the USDA soil texture classification.

Parameter	Clay	Silt	Loam	Sandy
Sand (%)	5	5	42	90
Silt (%)	5	90	41	5
Clay (%)	90	5	17	5
$n$	1.20	1.64	1.44	2.30
$pk_g$	12.5	12.3	12.8	11.4

However, gas permeability in unsaturated soils is also included in RP and varies significantly with %SSC and SWC. Increasing the water content in soils leads to a decrease in gas permeability, which influences RP, because the presence of water in porous materials decreases both the size of the pores and the effective porosity, and at the same time increases tortuosity [20]. The estimation of the unsaturated gas permeability,  $k_g(S_w)$ , can be formulated as follows (Equation (6)):

$$k_g(S_w) = k_g(1 - S_w^\tau) \cdot \left[ 1 - \left( 1 - \left( 1 - S_w^{m-1} \right)^m \right)^2 \right], \quad (6)$$

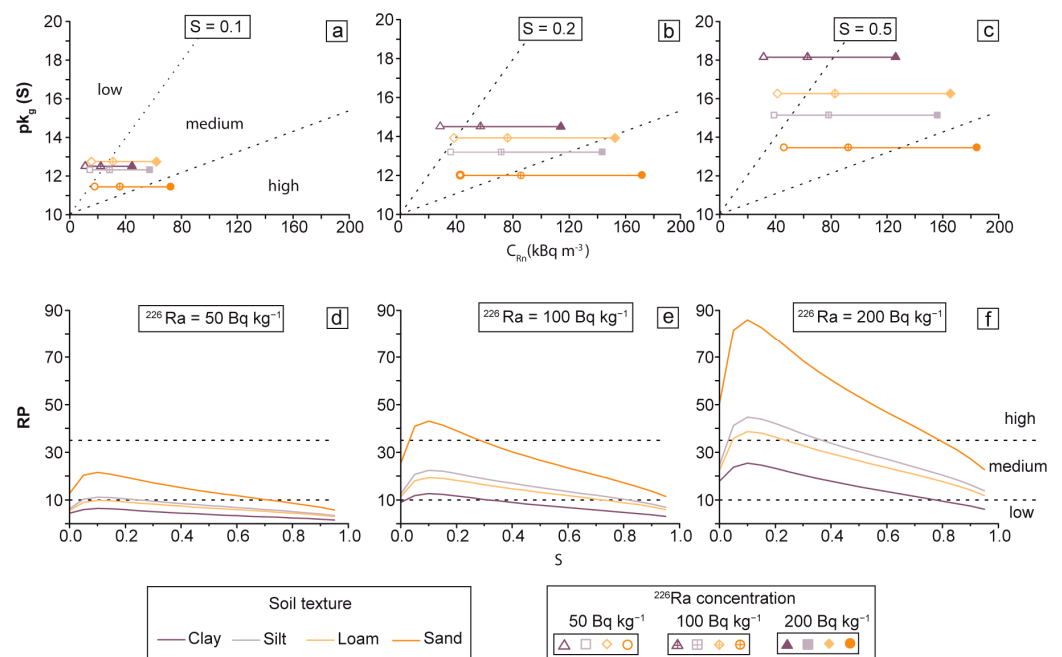
where  $k_g$  is the variable-saturated gas permeability,  $m$  results from the parameter  $n$  of the van Genuchten water retention curve as  $m = 1 - n^{-1}$ , and  $\tau$  is the tortuosity value (commonly  $\tau = 0.5$ ) [83]. Applying the approach proposed by [14] for RP studies,  $k_g$  and  $n$  are obtained from the Rosetta PTF using % SSC, together with the bulk density of the soil as input variables (Table 5).

Figure 9 analyses the impact of water content and soil texture on both radon activity and gas permeability (Figure 9a–c), as well as the radon potential (Figure 9d–f). This comparative analysis contemplates four different soils (clay, silt, loam, and sandy; Table 6) and three different <sup>226</sup>Ra activities, representing soils with low to high radon activity [12]. The calculations considered a bulk density of 1.7 g cm<sup>-3</sup>—a value corresponding to a loam soil—and a porosity of 0.5—an average value of the porosity of a soil—at 20 °C. Due to the emanation coefficient, radon activity strongly increases from  $S_w = 0$  to 0.1 (SWC = 0.05 for  $\phi = 0.5$ ) and remains nearly constant as water saturation increases. Relatively small fluctuations in water content at low values will lead to a high variability in radon concentration, as the long-term radon series also showed (Figures 2 and 3). As previously explained in Section 3.3, this variability is amplified with particle size (i.e., sandy soils). However, the changes in gas permeability are remarkable in clay soils, becoming more impermeable as water saturation increases (resulting in higher  $pk_g$  values; Figure 9a–c).

Water saturation influences RP evolution by changing radon activity and permeability (Figure 9d–f). As with radon activity, RP reaches its maximum at  $S_w = 0.1$  due to radon emanation. Therefore, small changes in SW (before reaching  $S_w = 0.1$ ) can result in RP rising from low to medium–high—e.g., hot desert climate—whereas RP decreases as water saturation increases due to the reduction in gas permeability. On the contrary, a water-saturated soil will present a low RP risk index—e.g., temperate oceanic climate.

This analysis emphasises the influence of weather parameters and soil characteristics on radon potential. Here, we have primarily evaluated soil water content, which is related to precipitation. However, barometric pressure, temperature, and wind can also affect radon potential and may make an accurate estimation difficult. This analysis particularly highlights how local soil texture heterogeneity can lead to significant variations in radon potential and risk index classification. Therefore, a comprehensive analysis of pedological properties such as soil structure, particle size distribution, water content distribution in the

soil profile, clay patches, organic matter, pH, etc., should be performed to better understand the dynamics of radon gas in soils and, consequently, radon potential classification.



**Figure 9.** Analysis of the impact of water content and soil texture on radon activity, gas permeability ( $pk_g$ ; (a–c)), and radon potential (RP; (d–f)). This comparative analysis contemplates four soil textures (clay, silt, loam, sandy) and three  $^{226}\text{Ra}$  concentrations (50–100–200  $\text{Bq kg}^{-1}$ ).

## 5. Conclusions

Long-term monitoring of loamy sand and silty clay loam soils highlights the importance of soil texture and weather parameters on radon dynamics. Rainfall plays a key role due to its direct impact on soil water content in the context of a warm semi-arid climate.

Statistical analysis of the time series reveals that radon activity undergoes strong seasonal variations related to rain and soil water content. For both soils, at the study depth of 90–100 cm, radon activity is above the average level during rainy periods, mainly in spring, whereas it is below these levels during dry periods, particularly in summer ( $4215 \pm 960 \text{ Bq m}^{-3}$  and  $1363 \pm 814 \text{ Bq m}^{-3}$ , in granite and calcareous soils, respectively). An increase in soil water content (SWC) enhances radon emanation. However, if this increase in SWC is high enough, the topsoil layer becomes saturated and impedes radon movement, causing a significant increase in radon activity.

For SWC to be significantly affected at a depth of 90–100 cm, there must be heavy and/or prolonged rainfall. Given these conditions, a measurable increase in SWC will occur much faster in the loamy sand soil compared to the silty clay loam soil. Radon increments due to SWC variation can be measurable within hours or days, depending on soil texture. Our artificial water experiments, which forced SWC to be higher than those usual in the studied region, demonstrate that humid climates with greater rainfall would result in soils with higher radon activities (for a given radium concentration).

Multivariate analysis reports how weather parameters determine the radon dynamics. SWC is likely to exert the most significant influence on radon in soil. However, its response to rainfall events and variability within the soil depth depends on the soil type. Barometric pressure, temperature, and wind also affect radon activity in soil, although their impact is less significant in the studied soils. Loamy sand soil shows statistically more robust results than silty clay loam soil. Thus, radon is positively related to SWC and negatively related to temperature, evapotranspiration, and pressure for both soils, while wind speed is only negatively associated with the loamy sand soil. Wavelet analysis confirms the

interrelation in the time–frequency domain of SWC and radon in loamy sand soil. In this soil, wavelet analysis also highlights the effect of variations in pressure and wind speed on radon activity. However, wavelet results for the silty clay loam are less decisive, probably due to the absence of rainfalls in the monitoring period, and also due to the inherent properties of the soil.

Finally, the analysis of the radon potential (RP) for the studied soils under a warm semi-arid climate is classified as low risk due to low  $^{226}\text{Ra}$  concentration. The response of radon activity to changes in the environment has been parametrised to model RP variations under different soils and climate conditions. Thus, theoretical RP analysis confirms the significant radon fluctuations recorded in the long-term radon series. Small fluctuations in water content at low soil VWC have a large impact on radon concentration, and afterwards, the activity remains stable. Water saturation influences RP evolution by changing radon activity and permeability applied to local soil texture heterogeneity and  $^{226}\text{Ra}$  concentration. Continuous monitoring is proven to be crucial for understanding seasonal radon changes, especially regarding the estimation of RP. Considering climate and weather variations and soil textures is essential not only for assessing RP and developing strategies for new buildings and mitigating possible radon risk hazards in existing constructions but also for creating more reliable large-scale radon risk maps.

**Author Contributions:** Conceptualisation, S.G.-O., C.P., J.V.-A. and D.B.; methodology, S.G.-O., C.P., J.V.-A. and D.B.; formal analysis, S.G.-O., C.P. and D.B.; investigation, S.G.-O., C.P., J.V.-A., A.F.-C. and D.B.; writing—original draft preparation, S.G.-O., C.P. and D.B.; writing—review and editing, S.G.-O., C.P., A.F.-C. and D.B.; visualisation, S.G.-O., C.P. and D.B.; supervision, C.P. and D.B.; project administration, D.B.; funding acquisition, D.B. All authors have read and agreed to the published version of the manuscript.

**Funding:** This research was funded by the Spanish Ministry of Science, Innovation and Universities, grant number RTI2018-099052-B-I00, and a pre-doctoral research fellowship (gran number PRE2019-088294) linked to this project.

**Institutional Review Board Statement:** Not applicable.

**Informed Consent Statement:** Not applicable.

**Data Availability Statement:** The data presented in this study are available on request from the corresponding author.

**Acknowledgments:** The authors wish to thank Geomnía Natural Resources SLNE for providing the soil samples used for the experiments; AM Rico-Amoros for supplying climatic data; LH Filiberto and N García-Martínez for their help in field and laboratory data acquisition; MC Ruiz for proofreading; K. Lewińska and C. Kazmierowski for laboratory assistance in soil characterisation; and VM García Perez for the technical assistance in sensor configuration of the experimental setup.

**Conflicts of Interest:** The authors declare no conflicts of interest. The funders had no role in the design of the study; in the collection, analyses, or interpretation of data; in the writing of the manuscript; or in the decision to publish the results.

## References

1. Barbosa, S.M.; Donner, R.V.; Steinitz, G. Radon Applications in Geosciences—Progress & Perspectives. *Eur. Phys. J. Spec. Top.* **2015**, *224*, 597–603.
2. Neri, M.; Ferrera, E.; Giammanco, S.; Currenti, G.; Cirrincione, R.; Patanè, G.; Zanon, V. Soil Radon Measurements as a Potential Tracer of Tectonic and Volcanic Activity. *Sci. Rep.* **2016**, *6*, 24581. [[CrossRef](#)] [[PubMed](#)]
3. Galiana-Merino, J.J.; Molina, S.; Kharazian, A.; Toader, V.E.; Moldovan, I.A.; Gómez, I. Analysis of Radon Measurements in Relation to Daily Seismic Activity Rates in the Vrancea Region, Romania. *Sensors* **2022**, *22*, 4160. [[CrossRef](#)] [[PubMed](#)]
4. World Health Organization. *WHO Handbook on Indoor Radon: A Public Health Perspective*; Zeeb, H., Shannoun, F., Eds.; WHO Press: Geneva, Switzerland, 2009; ISBN 9789241547673.
5. Darby, S.; Hill, D.; Auvinen, A.; Barros-Dios, J.M.; Baysson, H.; Bochicchio, F.; Deo, H.; Falk, R.; Forastiere, F.; Hakama, M.; et al. Radon in Homes and Risk of Lung Cancer: Collaborative Analysis of Individual Data from 13 European Case-Control Studies. *Br. Med. J.* **2005**, *330*, 223. [[CrossRef](#)] [[PubMed](#)]

6. Riudavets, M.; Garcia de Herrerros, M.; Besse, B.; Mezquita, L. Radon and Lung Cancer: Current Trends and Future Perspectives. *Cancers* **2022**, *14*, 3142. [[CrossRef](#)] [[PubMed](#)]
7. Neznal, M.; Neznal, M.; Matolín, M.; Barnet, I.; Miksova, J. *The New Method for Assessing the Radon Risk of Building Sites*; Czech Geological Survey: Prague, Czech Republic, 2004.
8. Beltrán-Torres, S.; Szabó, K.Z.; Tóth, G.; Tóth-Bodrogi, E.; Kovács, T.; Szabó, C. Estimated versus Field Measured Soil Gas Radon Concentration and Soil Gas Permeability. *J. Environ. Radioact.* **2023**, *265*, 107224. [[CrossRef](#)] [[PubMed](#)]
9. Gruber, V.; Bossew, P.; De Cort, M.; Tollefsen, T. The European Map of the Geogenic Radon Potential. *J. Radiol. Prot.* **2013**, *33*, 51–60. [[CrossRef](#)] [[PubMed](#)]
10. García-Talavera San Miguel, M.; López Acevedo, F.J. *Cartografía Del Potencial de Radón de España*; Colección Informes Técnicos 51.2019; Consejo de Seguridad Nuclear: Madrid, Spain, 2019.
11. Elío, J.; Crowley, Q.; Scanlon, R.; Hodgson, J.; Long, S. Logistic Regression Model for Detecting Radon Prone Areas in Ireland. *Sci. Total Environ.* **2017**, *599–600*, 1317–1329. [[CrossRef](#)] [[PubMed](#)]
12. European Commission; Joint Research Centre. *European Atlas of Natural Radiation*; Cinelli, G., De Cort, M., Tollefsen, T., Eds.; Publication Office of the European Union: Luxembourg, 2019; ISBN 9789276082590.
13. Petersell, V.; Täht-Kok, K.; Karimov, M.; Milvek, H.; Nirgi, S.; Raha, M.; Saarik, K. Radon in the Soil Air of Estonia. *J. Environ. Radioact.* **2017**, *166*, 235–241. [[CrossRef](#)]
14. Benavente, D.; Valdés-Abellán, J.; Pla, C.; Sanz-Rubio, E. Estimation of Soil Gas Permeability for Assessing Radon Risk Using Rosetta Pedotransfer Function Based on Soil Texture and Water Content. *J. Environ. Radioact.* **2019**, *208–209*, 105992. [[CrossRef](#)]
15. Aydar, E.; Diker, C. Carcinogen Soil Radon Enrichment in a Geothermal Area: Case of Güzelçamlı-Davutlar District of Aydın City, Western Turkey. *Ecotoxicol. Environ. Saf.* **2021**, *208*, 111466. [[CrossRef](#)] [[PubMed](#)]
16. Nicolas, A.; Girault, F.; Schubnel, A.; Pili, É.; Passelègue, F.; Fortin, J.; Deldicque, D. Radon Emanation from Brittle Fracturing in Granites under Upper Crustal Conditions. *Geophys. Res. Lett.* **2014**, *41*, 5436–5443. [[CrossRef](#)]
17. Sêco, S.L.R.; Domingos, F.P.; Pereira, A.J.S.C.; Duarte, L.V. Estimation of the Radon Production Potential in Sedimentary Rocks: A Case Study in the Lower and Middle Jurassic of the Lusitanian Basin (Portugal). *J. Environ. Radioact.* **2020**, *220–221*, 106272. [[CrossRef](#)] [[PubMed](#)]
18. Flexser, S.; Wollenberg, H.A.; Smith, A.R. Distribution of Radon Sources and Effects on Radon Emanation in Granitic Soil at Ben Lomond, California. *Environ. Geol.* **1993**, *22*, 162–177. [[CrossRef](#)]
19. Pla, C.; Cuezva, S.; Martinez-Martinez, J.; Fernandez-Cortes, A.; Garcia-Anton, E.; Fusi, N.; Crosta, G.B.; Cuevas-Gonzalez, J.; Cañaveras, J.C.; Sanchez-Moral, S.; et al. Role of Soil Pore Structure in Water Infiltration and CO<sub>2</sub> Exchange between the Atmosphere and Underground Air in the Vadose Zone: A Combined Laboratory and Field Approach. *Catena* **2017**, *149*, 402–416. [[CrossRef](#)]
20. Benavente, D.; Pla, C. Effect of Pore Structure and Moisture Content on Gas Diffusion and Permeability in Porous Building Stones. *Mater. Struct./Mater. Constr.* **2018**, *51*, 21. [[CrossRef](#)]
21. Chitra, N.; Bala Sundar, S.; Inigo Valan, I.; Subramanian, V.; Jose, M.T.; Venkatraman, B. Modeling and Experiments to Estimate Radon Emanation Factor in Soil-Grain Size and Moisture Effect. *Radiat. Prot. Dosim.* **2021**, *194*, 104–112. [[CrossRef](#)] [[PubMed](#)]
22. Scanlon, B.R.; Nicot, J.P.; Massmann, J.W. Soil Gas Movement in Unsaturated Systems. In *Soil Physics Companion*; Warrick, A.W., Ed.; CRC Press: Boca Raton, FL, USA, 2002.
23. Schery, S.D.; Gaeddert, D.H.; Wilkening, M.H. Factors Affecting Exhalation of Radon from Gravelly a Gravelly Sandy Loam. *J. Geophys. Res.* **1984**, *89*, 7299–7309. [[CrossRef](#)]
24. Sun, K.; Guo, Q.; Cheng, J. The Effect of Some Soil Characteristics on Soil Radon Concentration and Radon Exhalation from Soil Surface. *J. Nucl. Sci. Technol.* **2004**, *41*, 1113–1117. [[CrossRef](#)]
25. Thomas, P.A.; Anderson, D.W.; Zhang, W.; Baweja, A.S.; Tracy, B.L. Radon Emanation in Saskatchewan Soils. *Health Phys.* **2011**, *100*, 565–573. [[CrossRef](#)]
26. Ohno, M.; Okamoto, K.; Umegaki, K.; Fujiyoshi, R. Results of Simultaneous Monitoring of Soil <sup>222</sup>Rn and Moisture at Different Depths in a Forest Site in Fukushima Prefecture, Japan. *J. Radioanal. Nucl. Chem.* **2016**, *310*, 1013–1020. [[CrossRef](#)]
27. Ubeid, K.F.; Ramadan, K.A. Soil Types and Their Relations with Radon Concentration Levels in Middle Governorate of Gaza Strip, Palestine. *Pol. J. Soil Sci.* **2020**, *53*, 56–72. [[CrossRef](#)]
28. Asher-Bolinder, S.; Owen, D.E.; Schumann, R.R. Pedologic and Climatic Controls on RN-222 Concentrations in Soil Gas, Denver, Colorado. *Geophys. Res. Lett.* **1990**, *17*, 825–828. [[CrossRef](#)]
29. Tchorz-Trzeciakiewicz, D.E.; Rysiukiewicz, M. Ambient Gamma Dose Rate as an Indicator of Geogenic Radon Potential. *Sci. Total Environ.* **2021**, *755*, 142771. [[CrossRef](#)] [[PubMed](#)]
30. Gil-Oncina, S.; Valdes-Abellan, J.; Pla, C.; Benavente, D. Estimation of the Radon Risk Under Different European Climates and Soil Textures. *Front. Public Health* **2022**, *10*, 794557. [[CrossRef](#)]
31. Jackson, R.D. Diurnal Changes in Soil Water Content during Drying. In *Field Soil Water Regime*; Wiley: Hoboken, NJ, USA, 2015; pp. 37–55, ISBN 9780891189008.
32. Thomas, D.M.; Cotier, J.M.; Holford, D. Experimental Design for Soil Gas Radon Monitoring. *J. Radioanal. Nucl. Chem.* **1992**, *161*, 313–323. [[CrossRef](#)]
33. Siino, M.; Scudero, S.; Cannelli, V.; Piersanti, A.; D’Alessandro, A. Multiple Seasonality in Soil Radon Time Series. *Sci. Rep.* **2019**, *9*, 8610. [[CrossRef](#)] [[PubMed](#)]



34. Gavriliev, S.; Petrova, T.; Miklyaev, P. Factors Influencing Radon Transport in the Soils of Moscow. *Environ. Sci. Pollut. Res.* **2022**, *29*, 88606–88617. [[CrossRef](#)]
35. Voltaggio, M. Radon Progeny in Hydrometeors at the Earth's Surface. *Radiat. Prot. Dosim.* **2012**, *150*, 334–341. [[CrossRef](#)] [[PubMed](#)]
36. Sakoda, A.; Ishimori, Y.; Yamaoka, K. A Comprehensive Review of Radon Emanation Measurements for Mineral, Rock, Soil, Mill Tailing and Fly Ash. *Appl. Radiat. Isot.* **2011**, *69*, 1422–1435. [[CrossRef](#)]
37. Rey, N.G.; Dlott, D.D. Effects of Water on Low-Overpotential CO<sub>2</sub> Reduction in Ionic Liquid Studied by Sum-Frequency Generation Spectroscopy. *Phys. Chem. Chem. Phys.* **2017**, *19*, 10491–10501. [[CrossRef](#)]
38. Fujiyoshi, R.; Haraki, Y.; Sumiyoshi, T.; Amano, H.; Kobal, I.; Vaupotič, J. Tracing the Sources of Gaseous Components (<sup>222</sup>Rn, CO<sub>2</sub> and Its Carbon Isotopes) in Soil Air under a Cool-Deciduous Stand in Sapporo, Japan. *Environ. Geochem. Health* **2010**, *32*, 73–82. [[CrossRef](#)] [[PubMed](#)]
39. van der Laan, S.; van der Laan-Luijckx, I.T.; Zimmermann, L.; Conen, F.; Leuenberger, M. Net CO<sub>2</sub> Surface Emissions at Bern, Switzerland Inferred from Ambient Observations of CO<sub>2</sub>, δ(O<sub>2</sub>/N<sub>2</sub>), and <sup>222</sup>Rn Using a Customized Radon Tracer Inversion. *J. Geophys. Res.* **2014**, *119*, 1580–1591. [[CrossRef](#)]
40. Amundson, R.; Stern, L.; Baisden, T.; Wang, Y. The Isotopic Composition of Soil and Soil-Respired CO<sub>2</sub>. *Geoderma* **1998**, *82*, 83–114. [[CrossRef](#)]
41. Malczewski, D.; Żaba, J. <sup>222</sup>Rn and <sup>220</sup>Rn Concentrations in Soil Gas of the Izera Massif (Sudetes, Poland) as a Function of Sampling Depth. *Geol. Q.* **2017**, *61*, 877–886. [[CrossRef](#)]
42. Moreno, V.; Bach, J.; Font, L.; Baixeras, C.; Zarroca, M.; Linares, R.; Roqué, C. Soil Radon Dynamics in the Amer Fault Zone: An Example of Very High Seasonal Variations. *J. Environ. Radioact.* **2016**, *151*, 293–303. [[CrossRef](#)] [[PubMed](#)]
43. Seyis, C.; İnan, S.; Yalçın, M.N. Major Factors Affecting Soil Radon Emanation. *Nat. Hazards* **2022**, *114*, 2139–2162. [[CrossRef](#)]
44. Pulinets, S.; Mironova, I.; Miklyaev, P.; Petrova, T.; Shitov, A.; Karagodin, A. Radon Variability as a Result of Interaction with the Environment. *Atmosphere* **2024**, *15*, 167. [[CrossRef](#)]
45. Papachristodoulou, C.; Stamoullis, K.; Ioannides, K. Temporal Variation of Soil Gas Radon Associated with Seismic Activity: A Case Study in NW Greece. *Pure Appl. Geophys.* **2019**, *177*, 821–836. [[CrossRef](#)]
46. Haquin, G.; Zafir, H.; Ilzyer, D.; Weisbrod, N. Effect of Atmospheric Temperature on Underground Radon: A Laboratory Experiment. *J. Environ. Radioact.* **2022**, 253–254, 106992. [[CrossRef](#)]
47. Nassiri-Mofakham, N.; Kakaei, M.; Alavi, M. A Study on Radon Diffusion and Exhalation of Soils under Transient Conditions: Theoretical and Experimental Approach. *Appl. Radiat. Isot.* **2023**, *192*, 110616. [[CrossRef](#)] [[PubMed](#)]
48. Papachristodoulou, C.; Ioannides, K.; Spathis, S. The Effect of Moisture Content on Radon Diffusion through Soil: Assessment in Laboratory and Field Experiments. *Health Phys.* **2007**, *92*, 257–264. [[CrossRef](#)] [[PubMed](#)]
49. Chazarra Bernabé, A.; Lorenzo Mariño, B.; Romero Fresneda, R.; Moreno García, J.V. *Evolución de Los Climas de Köppen en España en el Periodo 1951–2020*; Agencia Estatal de Meteorología: Madrid, Spain, 2022.
50. *ISO 17892-4:2016*; Investigación y Ensayos Geotécnicos. Ensayos de Laboratorio de Suelos. Parte 4: Determinación de La Distribución Granulométrica. Asociación Española de Normalización (UNE): Madrid, Spain, 2019.
51. Topp, G.C.; Davis, J.L.; Annan, A.P. Electromagnetic Determination of Soil Water Content: Measurements in Coaxial Transmission Lines. *Water Resour. Res.* **1980**, *16*, 574–582. [[CrossRef](#)]
52. Alonso Hernández, H. *El Radón En Suelos, Rocas, Materiales de Construcción y Aguas*. Doctoral Thesis, Universidad de Las Palmas de Gran Canaria, Las Palmas, Spain, 2016.
53. Daubechies, I. Ten Lectures on Wavelets. *Math. Comput.* **1993**, *61*, 941–942. [[CrossRef](#)]
54. Kaiser, G. *A Friendly Guide to Wavelets*; Birkhäuser: Boston, MA, USA, 2011.
55. Wickerhauser, M.V. Adapted Wavelet Analysis from Theory to Software. *SIAM Rev.* **1996**, *38*, 160. [[CrossRef](#)]
56. Strang, G.; Nguyen, T. *Wavelets and Filter Banks*; Wellesley-Cambridge Press: Wellesley, MA, USA, 1997; ISBN 0-9614088-7-1.
57. D'Alessandro, A.; Scudero, S.; Siino, M.; Alessandro, G.; Mineo, R. Long-Term Monitoring and Characterization of Soil Radon Emission in a Seismically Active Area. *Geochem. Geophys. Geosyst.* **2020**, *21*, e2020GC009061. [[CrossRef](#)]
58. Galiana-Merino, J.J.; Pla, C.; Fernandez-Cortes, A.; Cuezva, S.; Ortiz, J.; Benavente, D. EnvironmentalWaveletTool: Continuous and Discrete Wavelet Analysis and Filtering for Environmental Time Series. *Comput. Phys. Commun.* **2014**, *185*, 2758–2770. [[CrossRef](#)]
59. Grinsted, A.; Moore, J.C.; Jevrejeva, S. Application of the Cross Wavelet Transform and Wavelet Coherence to Geophysical Time Series. *Nonlinear Process Geophys.* **2004**, *11*, 561–566. [[CrossRef](#)]
60. Arvela, H.; Holmgren, O.; Hänninen, P. Effect of Soil Moisture on Seasonalvariation in Indoor Radon Concentration: Modelling and Measurements in 326 Finnish Houses. *Radiat. Prot. Dosim.* **2016**, *168*, 277–290. [[CrossRef](#)]
61. İnan, S.; Kop, A.; Çetin, H.; Kulak, F.; Pabuçcu, Z.; Seyis, C.; Ergintav, S.; Tan, O.; Saatçılar, R.; Bodur, M.N. Seasonal Variations in Soil Radon Emanation: Long-Term Continuous Monitoring in Light of Seismicity. *Natural Hazards* **2012**, *62*, 575–591. [[CrossRef](#)]
62. Miklyaev, P.S.; Petrova, T.B.; Shchitov, D.V.; Sidiyakin, P.A.; Murzabekov, M.A.; Tsebro, D.N.; Marennyy, A.M.; Nefedov, N.A.; Gavriliev, S.G. Radon Transport in Permeable Geological Environments. *Sci. Total Environ.* **2022**, *852*, 158382. [[CrossRef](#)] [[PubMed](#)]
63. Pinault, J.L.; Baubron, J.C. Signal Processing of Soil Gas Radon, Atmospheric Pressure, Moisture, and Soil Temperature Data: A New Approach for Radon Concentration Modeling. *J. Geophys. Res. Solid Earth* **1996**, *101*, 3157–3171. [[CrossRef](#)]

64. Tareen, A.D.K.; Nadeem, M.S.A.; Kearfott, K.J.; Abbas, K.; Khawaja, M.A.; Rafique, M. Descriptive Analysis and Earthquake Prediction Using Boxplot Interpretation of Soil Radon Time Series Data. *Appl. Radiat. Isot.* **2019**, *154*, 108861. [[CrossRef](#)] [[PubMed](#)]
65. Naskar, A.K.; Akhter, J.; Gazi, M.; Mondal, M.; Deb, A. Impact of Meteorological Parameters on Soil Radon at Kolkata, India: Investigation Using Machine Learning Techniques. *Environ. Sci. Pollut. Res.* **2023**, *30*, 105374–105386. [[CrossRef](#)] [[PubMed](#)]
66. Chen, J.; Falcomer, R.; Ly, J.; Wierdsma, J.; Bergman, L. Long-Term Monitoring of Soil Gas Radon and Permeability at Two Reference Sites. *Radiat. Prot. Dosim.* **2008**, *131*, 503–508. [[CrossRef](#)] [[PubMed](#)]
67. Font, L.; Baixeras, C.; Moreno, V.; Bach, J. Soil Radon Levels across the Amer Fault. *Radiat. Meas.* **2008**, *43*, S319–S323. [[CrossRef](#)]
68. Kulali, F.; Akkurt, I.; Özgür, N. The Effect of Meteorological Parameters on Radon Concentration in Soil Gas. *Acta Phys. Pol. A* **2017**, *132*, 999–1001. [[CrossRef](#)]
69. Blazewicz, S.J.; Schwartz, E.; Firestone, M.K. Growth and Death of Bacteria and Fungi Underlie Rainfall-Induced Carbon Dioxide Pulses from Seasonally Dried Soil. *Ecology* **2014**, *95*, 1162–1172. [[CrossRef](#)] [[PubMed](#)]
70. Tan, S.; Ni, X.; Yue, K.; Liao, S.; Wu, F. Increased Precipitation Differentially Changed Soil CO<sub>2</sub> Efflux in Arid and Humid Areas. *Geoderma* **2021**, *388*, 114946. [[CrossRef](#)]
71. Sakoda, A.; Ishimori, Y.; Hanamoto, K.; Kataoka, T.; Kawabe, A.; Yamaoka, K. Experimental and Modeling Studies of Grain Size and Moisture Content Effects on Radon Emanation. *Radiat. Meas.* **2010**, *45*, 204–210. [[CrossRef](#)]
72. Dhar, S.; Randhawa, S.S.; Kumar, A.; Walia, V.; Fu, C.C.; Bharti, H.; Kumar, A. Decomposition of Continuous Soil–Gas Radon Time Series Data Observed at Dharamshala Region of NW Himalayas, India for Seismic Studies. *J. Radioanal. Nucl. Chem.* **2021**, *327*, 1019–1035. [[CrossRef](#)]
73. Yakut, H.; Tabar, E.; Yildirim, E.; Zenginerler, Z.; Ertugral, F.; Demirci, N. Soil Gas Radon measurement around Fault Lines on the Western Section of the North Anatolian Fault Zone in Turkey. *Radiat. Prot. Dosim.* **2017**, *173*, 405–413. [[CrossRef](#)]
74. Piersanti, A.; Cannelli, V.; Galli, G. The Pollino 2012 Seismic Sequence: Clues from Continuous Radon Monitoring. *Solid Earth* **2016**, *7*, 1303–1316. [[CrossRef](#)]
75. Turk, M.; Volarić, B.; Antolković, B. Radon Activity Concentration in the Ground and Its Correlation with the Water Content of the Soil. *Appl. Radiat. Isot.* **1996**, *47*, 377–381. [[CrossRef](#)]
76. Perrier, F.; Girault, F. Harmonic Response of Soil Radon-222 Flux and Concentration Induced by Barometric Oscillations. *Geophys. J. Int.* **2013**, *195*, 945–971. [[CrossRef](#)]
77. Bossew, P.; Cinelli, G.; Ciotoli, G.; Crowley, Q.G.; de Cort, M.; Medina, J.E.; Gruber, V.; Petermann, E.; Tollefsen, T. Development of a Geogenic Radon Hazard Index—Concept, History, Experiences. *Int. J. Environ. Res. Public Health* **2020**, *17*, 4134. [[CrossRef](#)] [[PubMed](#)]
78. Åkerblom, G. Ground Radon: Monitoring Procedures in Sweden. In Proceedings of the Radon Workshop, Geology, Environment, Technology, London, UK, 12 February 1993.
79. Giustini, F.; Ciotoli, G.; Rinaldini, A.; Ruggiero, L.; Voltaggio, M. Mapping the Geogenic Radon Potential and Radon Risk by Using Empirical Bayesian Kriging Regression: A Case Study from a Volcanic Area of Central Italy. *Sci. Total Environ.* **2019**, *661*, 449–464. [[CrossRef](#)] [[PubMed](#)]
80. Voltaggio, M.; Masi, U.; Spadoni, M.; Zampetti, G. A Methodology for Assessing the Maximum Expected Radon Flux from Soils in Northern Latium (Central Italy). *Environ. Geochem. Health* **2006**, *28*, 541–551. [[CrossRef](#)] [[PubMed](#)]
81. Zhuo, W.; Iida, T.; Furukawa, M. Modeling Radon Flux Density from the Earth’s Surface. *J. Nucl. Sci. Technol.* **2006**, *43*, 479–482. [[CrossRef](#)]
82. Zhuo, W.; Guo, Q.; Chen, B.; Cheng, G. Estimating the Amount and Distribution of Radon Flux Density from the Soil Surface in China. *J. Environ. Radioact.* **2008**, *99*, 1143–1148. [[CrossRef](#)]
83. Mualem, Y. A New Model for Predicting the Hydraulic Conductivity of Unsaturated Porous Media. *Water Resour. Res.* **1976**, *12*, 513–522. [[CrossRef](#)]

**Disclaimer/Publisher’s Note:** The statements, opinions and data contained in all publications are solely those of the individual author(s) and contributor(s) and not of MDPI and/or the editor(s). MDPI and/or the editor(s) disclaim responsibility for any injury to people or property resulting from any ideas, methods, instructions or products referred to in the content.